Broadband ^{13}C–^{13}C adiabatic mixing in solution optimized for high fields[☆]

Andrew E. Bennett, John D. Gross, and Gerhard Wagner[*]

Department of Biological Chemistry and Molecular Pharmacology, Harvard Medical School, 240 Longwood Avenue, Building C-1, Boston, MA 02115, USA

Abstract

Experiments which require mixing among spins with large frequency differences are generally performed with sequences based on composite pulses or computer-optimized cycles. Adiabatic pulses generally offer several advantages over other approaches, including greater single spin inversion bandwidths and tolerance to RF inhomogeneity. Here, a novel theoretical framework is presented in order to understand how spin–spin interactions are influenced by adiabatic inversion pulses, and insights from this approach are used to design more efficient adiabatic coherence exchange experiments. For very large frequency differences, this new approach generally offers improved results over previously applied mixing sequences, as applied to ^{13}C–^{13}C experiments which are the basis of modern sidechain assignment techniques in proteins. It is also anticipated that the approach presented here will be applicable to the analysis of various alternative approaches to adiabatic mixing.
© 2003 Published by Elsevier Inc.

1. Introduction

Multidimensional NMR experiments involving the exchange of coherences among spins are crucial to assigning resonances in complicated macromolecules [1]. The total correlation spectroscopy (TOCSY) [2] and homonuclear Hartmann–Hahn (HOHAHA) experiments [3] were introduced in order to obtain multiple relayed cross-peaks among ^{1}H spins. The advantage of this approach over COSY-type methods [1] is that a large number of in-phase correlations among spins can be observed in a single multidimensional experiment. The basic technique relies upon the application of a multiple pulse sequence to suppress chemical shift differences among spins and allow for exchange via the J interaction. In principle, a very strong spin lock field can accomplish this goal [2]. However, cycles consisting of composite inversion pulses are often used because they can compensate for the presence of significant frequency offsets within the

sample [4]. Provided that the RF field is strong compared to the frequency dispersion induced by chemical shifts, the effective two-spin Hamiltonian is reduced to just $H = J\vec{I}_1 \cdot \vec{I}_2$ over the multiple pulse cycle. In this limit, mixing is isotropic and magnetization exchange is equally efficient in all spatial dimensions. In conjunction with other techniques, broadband homonuclear mixing has become an important tool in assigning the chemical shifts of ^{1}H nuclei in macromolecules [5].

The HCCH–TOCSY experiment [6,7] and the HCCONH–TOCSY experiment [8–10] are extended versions of TOCSY which provide more efficient means of obtaining sidechain assignments using ^{13}C-labeled proteins, and these approaches are particularly useful for assigning randomly deuterated proteins. In HCCH–TOCSY, the coherence is relayed from ^{1}H spins to the directly attached ^{13}C nuclei and exchange occurs among the ^{13}C nuclei. In larger proteins, this approach has two important advantages. First, in proteins with many resonances and dense spectra, the approach can be applied as a three-dimensional (3D) experiment in which the ^{13}C frequency contributes an additional means of labeling the directly attached protons and provides ^{13}C assignments. A second important advantage of HCCH–TOCSY

---

is that the mixing step is mediated by *J*-couplings among ^{13}C spins, which are approximately 35–50 Hz, i.e., much larger than ^{1}H–^{1}H couplings. The HCCONH–TOCSY experiment is an important extension of HCCH–TOCSY in applications to larger proteins where HCCH–TOCSY is not applicable due to fast relaxation. In large deuterated proteins, HCCONH–TOCSY can take advantage of the excellent backbone resolution which is now available using relaxation-optimized (TROSY) experiments [11], and methyl groups can be assigned via selective ^{13}C-methyl group labeling and ^{13}C–^{13}C transfer across the otherwise deuterated side-chain [12,13].

Although several compensated trains of composite inversion pulses [4] have been applied to TOCSY exchange experiments [3,14], the "DIPSI" sequences have been among the most efficient and they are frequently employed [15,16]. The DIPSI sequences were developed using composite pulses with cyclic permutations in order to increase the bandwidth. For small resonance offsets, the effective Hamiltonian is an isotropic homonuclear *J* interaction. It was found that the exclusive use of 180° phase shifts led to the greatest bandwidth, compared with allowing 90° shifts as well [15]. Interestingly, however, these authors also determined that the effective Hamiltonian is somewhat less isotropic in sequences built only with 180° phase shifts. The flip–flop spectroscopy (FLOPSY) sequences [17,18] provide another approach that has a large mixing bandwidth, but FLOPSY sequences are not necessarily isotropic [18]. In addition, the FLOPSY approach is generally most suitable for longitudinal mixing [18]. This class of sequences was developed by computer optimization of the longitudinal mixing process, and in general the effective spin Hamiltonian is a mixture of zero-quantum terms. Both the FLOPSY and DIPSI sequences have been successfully applied to the mixing part of HCCH–TOCSY and HCCONH–TOCSY experiments and are commonly used to obtain the sidechain assignments of proteins.

More recently, adiabatic pulses [19–21] have been introduced into TOCSY experiments [22]. The advantages of adiabatic inversion pulses, which possess high bandwidth and tolerance with respect to radiofrequency (RF) inhomogeneity in the sample coil, make them attractive candidates for the building blocks of mixing pulse cycles [23]. In particular, adiabatic pulses have already been successfully applied in the case of the relatively narrow ^{1}H bandwidth [22]. Indeed, WURST-2 has been applied to the acquisition of "clean" TOCSY experiments [1], in which ^{1}H–^{1}H exchange due to cross-relaxation is greatly attenuated [24], and to magic angle spinning experiments on liquid samples in nanoprobes [25]. The WURST class of pulses, characterized by their wideband properties with uniform sweep rate and smooth truncation, is a flexible form of adiabatic pulse

in which the adiabaticity of the pulse can be scaled to different orders [26].

However, there have been relatively few demonstrations of how adiabatic pulses can be applied in ^{13}C–^{13}C mixing experiments. Peti et al. [27] have recently introduced adiabatic sequences based on tanh/tan pulses [28] which are efficient for ^{1}H–^{1}H TOCSY and can also be applied to ^{13}C–^{13}C mixing. WURST sequences can also be applied to ^{13}C–^{13}C mixing at 900 MHz [29]. Using computer simulations, Peti et al. also showed how the mixing efficiency varies with the resonance offsets δ_1 and δ_2 of two coupled spins in several adiabatic and composite pulse sequences. Compared to non-adiabatic sequences, the tendency for adiabatic sequences is to exhibit better bandwidth as a function of $\delta_1 + \delta_2$, while they behave less well as a function of the chemical shift difference $\Delta\delta = \delta_1 - \delta_2$ between two spins with chemical shifts δ_j [5,22,27].

In this paper, we develop an analytical approach to calculating the scaling factor of the *J*-coupling when a train of inversion pulses is applied. The scaling factor λ is a useful measure of mixing efficiency because exchange tends to occur as if the *J*-coupling were scaled according to $J \rightarrow \lambda J$ within the mixing bandwidth [5,30]. According to this definition, mixing is poor as $\lambda \rightarrow 0$, while it approaches maximum efficiency as $\lambda \rightarrow 1$. Our derivation reveals that the length of the adiabatic inversion pulse must be relatively short in order to obtain a high value of the scaling factor λ as a function of increasing chemical shift difference $\Delta\delta$. The fact that adiabatic pulses tend to be long is thus seen as a major reason for poor performance as a function of $\Delta\delta$, even when both interacting spins are efficiently inverted over a large bandwidth. Some analytical expressions for scaling factors have previously been introduced from the prospective of spin lock fields [5], but here a new approach is needed in order to evaluate the case of inversion pulse trains.

To develop useful sequences, we design adiabatic inversion pulses that maximize the bandwidth and tolerance for RF inhomogeneity but minimize the *J* scaling in accordance with practical constraints. Our approach initially involves a combination of numerical optimization of inversion pulses using an algorithm given by Rosenfeld et al. [31] and testing them in simulations of spin exchange. The shapes of optimal numerically derived pulses are also used to motivate an improved analytical shape, the "tan 40" pulse introduced below, a particular form of constant/tan pulse [32]. The analytical theory presented here is also extended to treat adiabatic pulses using the linear ramp ("chirp") pulse shape as a model system [33,34], and the effects of supercycling and finite pulse widths are briefly discussed. The analytical calculations are especially important in understanding the key factors in *J* scaling. In practice, in the case of widely separated ^{13}C resonances at high magnetic field,

our approach is an improvement over the performance of FLOPSY sequences, even at the relatively low RF powers of 7–8 kHz which are routinely applied in many laboratories.

2. Theory

An ideal sequence for mixing among spins separated by large frequency shifts, such as ^{13}C–^{13}C nuclei, must satisfy several conflicting criteria simultaneously. The basic Hamiltonian for the J-coupled spin pair in the presence of an RF field is the following:

$$H(t) = \delta_1 I_{z1} + \delta_2 I_{z2} + J[I_{x1}I_{x2} + I_{y1}I_{y2} + I_{z1}I_{z2}] + H_{RF}(t). \tag{2.1}$$

The time-dependent RF field of maximum amplitude ν_{RF} must suppress large chemical shifts δ_1 and δ_2 in order to recover the full J-coupling [5].

Here, we consider sequences with trains of inversion pulses. Although an adiabatic pulse tends to offer exceptional bandwidth, the adiabaticity condition is approached only as the length of the pulse is increased. Accordingly adiabatic pulses are generally long compared to other inversion pulses delivered at the same average RF power level. On the other hand, as shown here, the degree to which the J-coupling is effectively scaled down by the pulse sequence depends critically on the interpulse spacing τ. As τ is made shorter, more efficient mixing is attained provided that the inversion pulses are sufficiently adiabatic and provide satisfactory spin inversion. Therefore, there is a conflict between meeting the adiabatic condition and applying the pulses at the fastest possible rate in order to avoid undesirable scaling of the J interaction.

The approach pursued here consists of optimizing adiabatic pulses with numerical techniques and incorporating them into mixing supercycles. The supercycles applied here mostly consist of MLEV cycles [4] of P5 inversion elements [35] with XY expansions [36]. The combination of MLEV and P5 has already been shown to aid in mixing efficiency [22,27]. The XY permutation eliminates undesirable double-quantum interactions from the final effective spin Hamiltonian (see Section 2.5). The sequences used in this thesis were mostly constructed with pulses that are rendered as short as possible with a computational optimization procedure and the guidance of the analytical theory introduced here. Because of its generality and ease of implementation, we chose the optimization procedure of Rosenfeld et al. [31] for the design of individual pulses. Their algorithm was used to optimize pulses for the desired bandwidth and a given tolerance with respect to RF field inhomogeneity. We have been most successful with constant amplitude adiabatic pulses, which are pursued

below, primarily because of their favorable chemical shift scaling properties. However, various amplitude modulation schemes can be applied with numerical optimization.

2.1. Theory of exchange with ideal inversion pulses

In this section, an analytical approach is developed for longitudinal mixing in a homonuclear spin pair undergoing a sequence of δ-function π pulses. One pulse is applied per time period τ. This problem can be solved analytically to an excellent approximation in the limit of weak spin–spin coupling (as is strongly obeyed here), and it provides insight into the relationship between interpulse spacing and the scaling of the J-coupling.

At times $t = (n + 1/2)\tau$, a sudden π rotation is imposed by the RF field. After conversion into both the rotating and toggling frame, the internal Hamiltonian can be written in the following form:

$$\tilde{H}(t) = \delta_1 \Phi(t) I_{z1} + \delta_2 \Phi(t) I_{z2} \\ + J[I_{x1}I_{x2} + I_{y1}I_{y2} + I_{z1}I_{z2}]. \tag{2.2}$$

The function $\Phi(t)$ characterizes sudden spin flips imposed by the infinitely short π pulses. It equals +1 after an even number of π pulses, −1 after an odd number [37]. RF fields that are applied to both spins do not directly affect the homonuclear J interaction. The toggling frame Hamiltonian of Eq. (2.2) can be written as the sum of the following two commuting terms:

$$\tilde{H}(t) = \tilde{H}_0^{14}(t) + \tilde{H}_0^{23}(t), \tag{2.3}$$

using the definitions:

$$\tilde{H}_0^{14}(t) = \{\delta_1 + \delta_2\}\Phi(t)\tfrac{1}{2}[I_{z1} + I_{z2}] + JI_{z1}I_{z2},$$
$$\tilde{H}_0^{23}(t) = \{\delta_1 - \delta_2\}\Phi(t)\tfrac{1}{2}[I_{z1} - I_{z2}] + J[I_{x1}I_{x2} + I_{y1}I_{y2}]. \tag{2.4}$$

This partitioning of the Hamiltonian is convenient because the terms commute with each other at all times [38].

The longitudinal component of the J interaction, $JI_{1z}I_{2z}$, also commutes with the rest of the Hamiltonian at all times, even in the toggling frame, and does not participate in the dynamics at all. However, more complicated spin dynamics occur in the 23-subspace of the Hamiltonian [36], which can be partitioned into two non-commuting terms $\tilde{H}^{23}(t) = \tilde{H}_0^{23}(t) + \tilde{H}_1^{23}(t)$:

$$\tilde{H}^{23}(t) = \tilde{H}_0^{23}(t) + \tilde{H}_1^{23}(t) \\ = \{\delta_1 - \delta_2\}\Phi(t)\tfrac{1}{2}[I_{z1} - I_{z2}] + J[I_{x1}I_{x2} + I_{y1}I_{y2}], \tag{2.5}$$

where

$$\tilde{H}_0^{23}(t) = \{\delta_1 - \delta_2\}\Phi(t)\tfrac{1}{2}[I_{z1} - I_{z2}],$$
$$\tilde{H}_1^{23}(t) = J[I_{x1}I_{x2} + I_{y1}I_{y2}]. \tag{2.6}$$

This component of the Hamiltonian has been called the 23-subspace [38] because it characterizes dynamics between the second and third quantum states of the two-spin system when they are expressed as eigenstates of both I_{z1} and I_{z2}. The Hamiltonians $\tilde{H}_0^{23}(t)$ and $\tilde{H}_1^{23}(t)$ do not commute, so $\tilde{H}^{23}(t)$ is not diagonal and it is the portion where complex dynamics like spin exchange occur. In contrast, $\tilde{H}^{14}(t)$ is diagonal and always commutes with $\tilde{H}^{23}(t)$.

The division of the Hamiltonian into $\tilde{H}_0^{23}(t)$ and $\tilde{H}_1^{23}(t)$ enables the definition of a second toggling frame in the following way:

$$U(\tau,0) = U_0(\tau,0) \exp\left\{ -\mathrm{i} \int_0^\tau \mathrm{d}t\, U_0^{-1}(t,0)\tilde{H}_1(t)U_0(t,0) \right\},$$
(2.7)

where

$$U_0(\tau,0) = \exp\left\{ -\mathrm{i} \int_0^\tau \mathrm{d}t\, (\delta_1 - \delta_2)\Phi(t)[I_{z1} - I_{z2}] \right\}$$

and $U_0(\tau,0)$ is the time propagator.

These expressions motivate the definition of a second interaction frame [39]:

$$\tilde{\tilde{H}}_1^{23}(t) = U_0^{-1}(t,0)\tilde{H}_1^{23}(t)U_0(t,0).$$
(2.8)

With the further definition of the phase factor

$$\chi(t) = \int_0^t \mathrm{d}t'\, (\delta_1 - \delta_2)\Phi(t')$$
(2.9)

the J-coupling interaction in the second toggling frame can be written:

$$\begin{aligned}\tilde{\tilde{H}}_1(t) &= J\cos\chi(t)\left[I_{x1}I_{x2} + I_{y1}I_{y2}\right]\\ &\quad + J\sin\chi(t)\left[I_{y1}I_{x2} - I_{x1}I_{y2}\right].\end{aligned}$$
(2.10)

After each pair of π pulses, the second term in Eq. (2.10) vanishes because the first pulse flips the sign of the second zero-quantum operator $[I_{y1}I_{x2} - I_{x1}I_{y2}]$. The explicit form of Eq. (2.9) for the δ-function π pulse is substituted into Eq. (2.10) and integrated to obtain the zero-order term in the Magnus expansion, i.e., the Average Hamiltonian approximation [40]:

$$\begin{aligned}\tilde{\tilde{H}}_1^{(0)} &= \frac{1}{\tau}\int_0^\tau \mathrm{d}t\, \tilde{\tilde{H}}_1(t)\\ &= J\left\{\frac{1}{\tau}\int_0^\tau \mathrm{d}t\, \cos\chi(t)\right\}\left[I_{x1}I_{x2} + I_{y1}I_{y2}\right].\end{aligned}$$
(2.11)

Because the J term is small, and the chemical shift terms are cyclic at times $t = n\tau$ in the sense that $\chi(n\tau) = 0$, so that $U_0(n\tau,0) = \pm 1$. Accordingly, the average Hamiltonian approximation can be used to approximate the total effective J-coupling as follows:

$$\tilde{\tilde{H}}_1^{(0)} = J I_{z1}I_{z2} + J\left\{\frac{2}{\Delta\delta\tau}\sin\left(\frac{\Delta\delta\tau}{2}\right)\right\}\left[I_{x1}I_{x2} + I_{y1}I_{y2}\right],$$
(2.12)

where τ is the delay between the π pulses and $\mathrm{Dd} = \mathrm{d}_1 - \mathrm{d}_2$. Since the term $J I_{z1}I_{z2}$ commuted with the rest of the Hamiltonian at all times in the toggling frame, it can be restored here. The longitudinal term is not scaled by the π pulses, and in the most general case Eq. (2.12) is not isotropic. Within the model of δ-function π pulses given here, the analytical expression for the scaled J-coupling is quantitatively accurate in the limit of small J compared to the RF field. This condition is strongly obeyed in high resolution solution experiments.

The full J interaction is recovered if and only if $\Delta\delta\tau \ll 1$. This places an upper bound on the length of the π pulse. Otherwise, if the rate of pulsing is not rapid compared to the chemical shift difference between the spins, there is extensive scaling of the zero-quantum term in Eq. (2.12), which is defined by

$$\{I_{x1}I_{x2} + I_{y1}I_{y2}\} = 1/2\{I_{+1}I_{-2} + I_{-1}I_{+2}\}.$$
(2.13)

When not excessively scaled, this term can be used to generate longitudinal mixing. In the limit of small $\Delta\delta = \delta_1 - \delta_2$, the coupling becomes isotropic. However, under realistic experimental conditions we will expect significant chemical shift scaling of the zero-quantum terms, while the $I_{z1}I_{z2}$ term is relatively unaffected.

When isotropic symmetry is broken in this fashion, the best option conceptually is longitudinal mixing. Likewise, in the limit of large resonance offsets, exchange efficiencies are highly unequal along different dimensions in DIPSI experiments, even though the Hamiltonian is isotropic in the limit of small spin frequencies. As resonance offsets increase, Fig. 1 illustrates simulations which show that DIPSI-3 is most suitable for in-phase transverse coherence exchange, while out-of-phase transverse mixing performs poorly, as one example of anisotropic behavior. The FLOPSY approach operates best in the setting of longitudinal mixing [17].
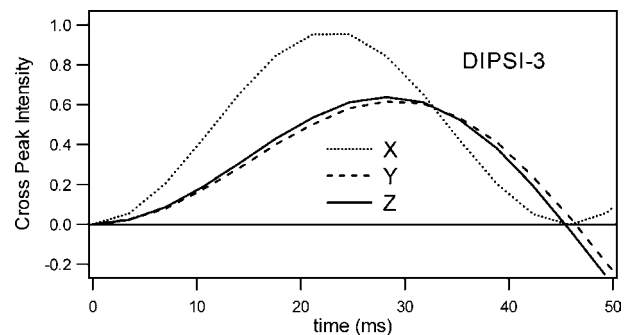

Fig. 1. Simulation of DIPSI-3 mixing between two spins as a function of the initial spin state. The pulses are all applied along the X-axis in the rotating frame. The spin frequencies are separated by $\Delta\delta = 7\,\mathrm{kHz}$ and the applied RF field is 7.7 kHz. The most important feature is the anisotropy of the mixing efficiency, namely that signal decays along the directions which are orthogonal to the phases of the RF pulses. In contrast, FLOPSY and the adiabatic sequences based on inversion pulses are most efficient along Z.

In a general way, it seems likely that relaxation effects may favor longitudinal mixing over in-phase transverse mixing. However, a highly robust mixing approach which offers equivalent in-phase and out-of-phase transverse mixing could be the best approach because of the advantage of sensitivity enhancement [1]. In this article, adiabatic exchange experiments are shown only for the case of longitudinal mixing, but transverse mixing with sensitivity enhancement may be possible with improved sequences at relatively high RF powers.

2.2. Theory of exchange with adiabatic pulses

Fig. 2 illustrates two adiabatic frequency sweeps applied in our experiments. The first is a numerically derived pulse, the second a linear ramp "chirp" pulse [33]. These pulses are suitable for mixing at 500 MHz magnetic field. Fig. 3 compares the scaling factor of the J-interaction as a function of the chemical shift difference $\Delta\delta = \delta_1 - \delta_2$ between the spins for the two waveforms. Fig. 3 compares the performance of the δ-function π pulse approximation developed in Section 2.1 with exact calculations of the scaling factor λ for the numerical and linear adiabatic pulses at the same pulsing rate. The plots illustrate that the δ-function π pulse approximation is qualitatively correct, but it overestimates how much the coupling is scaled down. The main reason is that the continuous application of RF power acts to reduce the effective chemical shift difference. Here we modify the π pulse treatment to correct the scaling factor for the effect of finite pulse length. Curves for the approach presented in this section, also shown in Fig. 3, illustrate that this approach can make quantitative predictions over a large bandwidth.
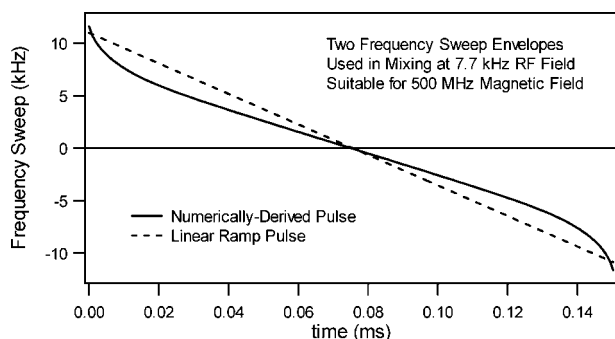

Fig. 2. Adiabatic pulse envelopes designed initially for use at 500 MHz. The numerical algorithm of Rosenfeld and co-workers discussed in the text was applied to design the frequency sweep, shown as a solid line. A similar linear ramp pulse which was optimized by computer simulations of mixing for field strengths at 500 MHz is also shown, and it is only moderately less efficient than the numerically derived pulse in simulations. For these pulses, the intended RF amplitude is 7.7 kHz to cover a 7 kHz bandwidth.
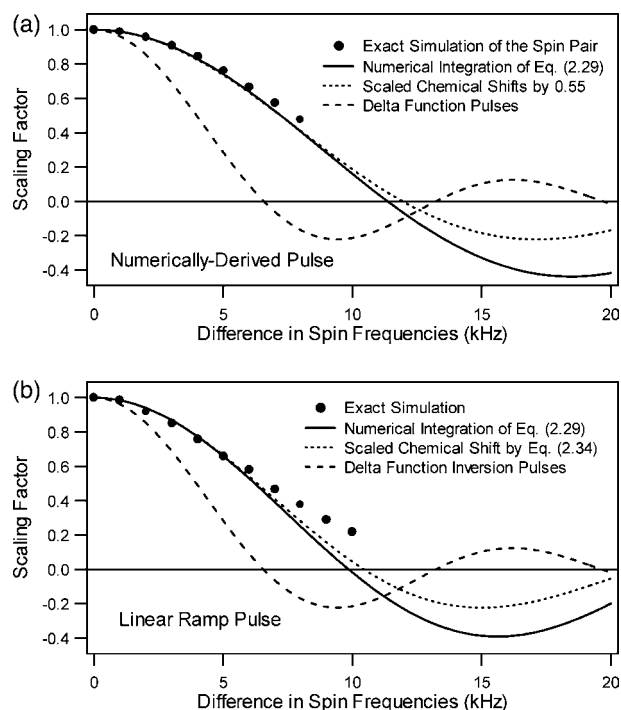

Fig. 3. Comparisons of the scaling factor of the J-coupling given by the analytical theory and contrasted with simulations. In part (a), the behavior of the numerical pulse in Fig. 2 is examined. A train of δ-function pulses (long dashes) is seen to yield much less efficiency at the same rate of pulsing, i.e., one π pulse applied every 151 μs. The dots illustrate the scaling factor recovered from exact simulations of the spin pair. Numerical integration of Eq. (2.29), shown as a solid line, and a simple model of scaled chemical shifts, according to $\Delta\delta_{\text{eff}} \rightarrow 0.55 \cdot \Delta\delta$, (short dashes) yield excellent agreement with the exact calculation. Exact data is not shown beyond $\Delta\delta = 8$ kHz because the numerically derived adiabatic pulse was not designed to operate there. Similar results are seen from the linear ramp pulse in part (b), with the difference that in this case there is an analytical expression for the chemical shift scaling factor, given by Eq. (2.34), which yields $\alpha = 0.62$. Beyond $\Delta\delta = 10$ kHz a single exchange frequency is not well defined in the exact two spin calculations.

Our analytical model assumes ideal adiabaticity. The Hamiltonian describing the interaction of the adiabatic pulse with the homonuclear spin pair is the following:

$$H(t) = \{\delta(t) + \delta_1\}I_{z1} + v_{\text{RF}}(t)I_{x1} + \{\delta(t) + \delta_2\}I_{z2} + v_{\text{RF}}(t)I_{x2} + J[I_{x1}I_{x2} + I_{y1}I_{y2} + I_{z1}I_{z2}], \quad (2.14)$$

where $\delta(t)$ and $v_{\text{RF}}(t)$ describe the adiabatic sweep.

It is convenient to apply a time-dependent transformation of the angular momentum operators in order to restate the Hamiltonian as follows:

$$H(t) = \sqrt{(\delta(t) + \delta_1)^2 + v_{\text{RF}}^2(t)}\hat{I}_{z1} + \sqrt{(\delta(t) + \delta_2)^2 + v_{\text{RF}}^2(t)}\hat{I}_{z1} + J[I_{x1}I_{x2} + I_{y1}I_{y2} + I_{z1}I_{z2}], \quad (2.15)$$

where

$$\hat{I}_{zj}(t) = I_{zj}\cos\theta_j(t) + I_{xj}\sin\theta_j(t). \quad (2.16)$$

For convenience we also define the phase angles

$$\cos \theta_j(t) = \frac{\delta(t) + \delta_j}{\sqrt{(\delta(t) + \delta_j)^2 + v_{\mathrm{RF}}^2(t)}},$$

$$\sin \theta_j(t) = \frac{v_{\mathrm{RF}}(t)}{\sqrt{(\delta(t) + \delta_j) + v_{\mathrm{RF}}^2(t)}}. \tag{2.17}$$

It is also helpful to define analogous transformations where $\delta_j = 0$. These are denoted by $\hat{I}_{zj}(t) = I_{zj} \cos \theta(t) + I_{xj} \sin \theta(t)$ and the following analogues

$$\cos \theta(t) = \frac{\delta(t)}{\sqrt{\delta^2(t) + v_{\mathrm{RF}}^2(t)}},$$

$$\sin \theta(t) = \frac{v_{\mathrm{RF}}(t)}{\sqrt{\delta^2(t) + v_{\mathrm{RF}}^2(t)}}. \tag{2.18}$$

The related transformations along other directions are given by $\hat{I}_{xj}(t) = I_{xj} \cos \theta(t) - I_{zj} \sin \theta(t)$ and $\hat{I}_{yj}(t) = I_{yj}$. For simplicity, the time-dependence of these tilted axis systems is not written explicitly in most cases.

We specialize to the case of relatively small resonance offsets which obey the condition $\delta_j \ll \sqrt{\delta^2(t) + v_{\mathrm{RF}}^2(t)}$. This constraint applies to our experiments, and indeed if it is violated, poor scaling factors are likely to result. For relatively small resonance offsets, the following approximation can be applied via series expansion of the square root (through first order):

$$\sqrt{(\delta(t) + \delta_j)^2 + v_{\mathrm{RF}}^2(t)} \approx \sqrt{\delta^2(t) + v_{\mathrm{RF}}^2(t)} + \frac{\delta(t)}{\sqrt{\delta^2(t) + v_{\mathrm{RF}}^2(t)}} \delta_j. \tag{2.19}$$

Likewise, when the chemical shifts δ_j are small, the tilted axis systems $(\hat{I}_{xj}, \hat{I}_{yj}, \hat{I}_{zj})$ are similar for both spins $j = 1, 2$ and approximately equivalent to the common rotation system $(\hat{\hat{I}}_{xj}, \hat{\hat{I}}_{yj}, \hat{\hat{I}}_{zj})$. With these approximations, the Hamiltonian then becomes:

$$H(t) \approx \sum_j \left\{ \sqrt{\delta^2(t) + v_{\mathrm{RF}}^2(t)} + \frac{\delta(t)}{\sqrt{\delta^2(t) + v_{\mathrm{RF}}^2(t)}} \delta_j \right\} \hat{\hat{I}}_{zj}$$
$$+ J\vec{I}_1 \cdot \vec{I}_2. \tag{2.20}$$

More rigorously, the Hamiltonian given by Eq. (2.14) can be rewritten exactly in terms of the common axis system $(\hat{\hat{I}}_{xj}, \hat{\hat{I}}_{yj}, \hat{\hat{I}}_{zj})$, which contributes additional rotations involving the tilted X-axis:

$$H(t) = \sqrt{\delta^2(t) + v_{\mathrm{RF}}^2(t)} \left\{ \hat{\hat{I}}_{z1} + \hat{\hat{I}}_{z2} \right\}$$
$$+ \sum_j \cos \theta(t) \delta_j \hat{\hat{I}}_{zj}$$
$$- \sum_j \sin \theta(t) \delta_j \hat{\hat{I}}_{xj} + J\vec{I}_1 \cdot \vec{I}_2. \tag{2.21}$$

The first term is just the Hamiltonian of the RF field, and under adiabatic conditions the path of the angular momentum operators $\hat{\hat{I}}_{zj}$ is identical to the trajectory of Zeeman magnetization under the influence of the pulse:

$$U_{\mathrm{RF}} I_{zj} U_{\mathrm{RF}}^{-1} = \hat{\hat{I}}_{zj}. \tag{2.22}$$

With the definition

$$H_{\mathrm{RF}}(t) = \sqrt{\delta^2(t) + v_{\mathrm{RF}}^2(t)} \{ \hat{\hat{I}}_{z1}(t) + \hat{\hat{I}}_{z2}(t) \},$$

adiabaticity yields:

$$U_{\mathrm{RF}}^{-1} \hat{\hat{I}}_{zj} U_{\mathrm{RF}} = I_{zj}. \tag{2.23}$$

On the other hand, the terms involving $\hat{\hat{I}}_{xj}$ contribute much less than the $\hat{\hat{I}}_{zj}$ terms because they do not commute with the RF field. The behavior of the $\hat{\hat{I}}_{xj}$ terms under RF modulation is complex because the mutual spin axis system $(\hat{\hat{I}}_{xj}, \hat{\hat{I}}_{yj}, \hat{\hat{I}}_{zj})$ is undergoing rotation. This system has been defined such that $\hat{\hat{I}}_{zj}(t)$ is the path of the RF field in the rotating frame. This path is the same as the rotation of longitudinal coherence under adiabatic conditions, and its rate of change is by definition slow compared to the frequency of precession induced by the effective RF field vector.

Therefore, on a time scale that is short compared to the length of the adiabatic pulse, we can omit the Dyson time-ordering operator T from the propagator for the RF pulses,

$$U_{\mathrm{RF}}(t,0) = T \exp \left\{ -\mathrm{i} \int_0^t \mathrm{d}t' \left[\sqrt{\delta^2(t') + v_{\mathrm{RF}}^2(t')} \times \left(\hat{\hat{I}}_{z1}(t') + \hat{\hat{I}}_{z2}(t') \right) \right] \right\}$$

and write

$$U_{\mathrm{RF}}^{-1} \hat{\hat{I}}_{xj} U_{\mathrm{RF}} = \hat{\hat{I}}_{xj} \cos \left\{ \int_0^t \mathrm{d}t' \sqrt{\delta^2(t') + v_{\mathrm{RF}}^2(t')} \right\}$$
$$+ \hat{\hat{I}}_{yj} \sin \left\{ \int_0^t \mathrm{d}t' \sqrt{\delta^2(t') + v_{\mathrm{RF}}^2(t')} \right\}. \tag{2.24}$$

With sufficient separation of time scales between the rate of tilt in the adiabatic trajectory and the precession period, this approximate result indicates that the $\hat{\hat{I}}_{xj}$ terms are greatly scaled down in the toggling frame to $\mathrm{O}\{\delta_j / \sqrt{\delta^2(t) + v_{\mathrm{RF}}^2(t)}\}$. Interestingly, although this separation of time scales is not always strongly obeyed by the sequences discussed in this paper, it is nonetheless the case that this term contributes little to the calculated scaling factor over most of the bandwidth. With the above results in mind, the complete propagator can be approximated in the toggling frame as follows:

$$U = U_{\mathrm{RF}} \exp \left\{ -\mathrm{i} \int_0^\tau \mathrm{d}t \left[\sum_j \cos \theta(t) \delta_j U_{\mathrm{RF}}^{-1} \hat{\hat{I}}_{zj} U_{\mathrm{RF}} \right. \right.$$
$$\left. \left. + \sum_j \sin \theta(t) \delta_j U_{\mathrm{RF}}^{-1} \hat{\hat{I}}_{xj} U_{\mathrm{RF}} + J\vec{I}_1 \cdot \vec{I}_2 \right] \right\}. \tag{2.25}$$

The J-coupling is not directly affected by identical simultaneous rotations of both homonuclear spins. With the assumption of adiabaticity, the propagator simplifies to an expression that is analogous to Eq. (2.2):

$$U = U_{RF} \exp \left\{ -I \int_0^\tau dt \sum_j \cos\theta(t) \delta_j I_{zj} + J\vec{I}_1 \cdot \vec{I}_2 \right\}.$$
(2.26)

Again within the toggling frame, the effective spin Hamiltonian has the simplified form: $\tilde{H}(t) = \cos\theta(t)\,\delta_1 I_{z1} + \cos\theta(t)\delta_2 I_{z2} + \vec{I}_1 \cdot \vec{I}_2$. Although the adiabatic trajectory is more complex than that of an ideal π pulse, the components of Eq. (2.26) obey the same commutation relationships seen in Eq. (2.2) and can be treated in a similar fashion.

We define a phase factor involving modulation of the flip–flop component of the J-coupling:

$$\chi(t) = \int_0^t dt'\,(\delta_1 - \delta_2) \frac{\delta(t)}{\sqrt{\delta^2(t) + v_{RF}^2(t)}}.$$
(2.27)

With this definition, the scaling factor can be defined as follows:

$$\tilde{\bar{H}}_1^{(0)} = JI_{z1}I_{z2} + \lambda J\left[I_{x1}I_{x2} + I_{y1}I_{y2}\right],$$
(2.28)

where:

$$\lambda = \frac{1}{\tau} \int_0^\tau dt \cos\left\{ \int_0^t dt'(\delta_1 - \delta_2) \frac{\delta(t')}{\sqrt{\delta^2(t') + v_{RF}^2(t')}} \right\}.$$
(2.29)

The length of the adiabatic pulse is given by τ. In most cases, this integral cannot be solved analytically. However, Eq. (2.29) is easy to calculate numerically. An approximate solution for chirp pulses is provided in Section 2.4. In Fig. 3, it is clear that the approximation expressed by Eqs. (2.28) and (2.29) is excellent for the two example waveforms.

More generally, Eq. (2.29) is important because it demonstrates a key determinant of the scaling factor. In Section 1, we saw that one important factor is how short the pulse can be made compared to the resonance offsets δ_j of the spins. We see here that it is also advantageous to apply the adiabatic trajectory in such a way as to maximize the scaling of chemical shifts according to $\delta_j \rightarrow \cos\theta(t)\delta_j$. These considerations imply it is best to minimize the breadth of the frequency sweep in order to achieve favorable scaling properties. In the case of a linear ramp of the form $\delta(t) = \delta_{max} - kt$, for example, chemical shift scaling increases as δ_{max} is reduced, and consequently the scaling factor λ increases.

2.3. Numerical adiabatic pulse optimization

Motivated by the result of Eq. (2.12), we sought a flexible algorithm for developing relatively short adiabatic pulses and testing them for mixing applications. We chose the algorithm of Rosenfeld et al. [31], which optimizes the timing of an adiabatic inversion pulse within a semi-elliptical trajectory. This method and similar ones [41] have been frequently applied to the development of adiabatic pulses for imaging applications. For RF fields applied along the X-axis in the rotating frame, the trajectory in the XZ-plane is set by the user [31]. In particular, the user defines the functions $f\{\eta(t)\}$ and $g\{\eta(t)\}$ that define the trajectory of the pulse within the XZ-plane of the rotating frame:

$$H_{RF}(t) = f\{\eta(t)\}I_z + g\{\eta(t)\}I_x.$$
(2.30)

The I_z term defines the frequency sweep of the pulse, while the transverse term I_x defines an envelope of amplitude modulation. For inversion pulses, arbitrary phase modulation can be redefined as frequency modulation without loss of generality, so no I_y term is needed. The boundary conditions of Eq. (2.29) are $|f\{\pm\pi/2\}| \gg |g\{\pm\pi/2\}|$, $f\{-\pi/2\} > 0$, and $f\{\pi/2\} < 0$. These are implicitly defined by the user, and they constrain the sweep to begin at a large positive frequency and rotate the effective RF field in the rotating frame across the transverse plane into a large negative frequency. This trajectory accomplishes spin inversion if performed adiabatically. Specific inputs therefore include the maximum RF field amplitude v_{RF}, as well as the initial and final frequencies of the sweep (δ_{min} and $\delta_{max} = -\delta_{min}$). The total sweep width is therefore $2\delta_{max}$. The user also enters a desired range of offset and RF inhomogeneity compensation. The method of Rosenfeld et al. applied here calculates the pulse timing trajectory $\eta(t)$ by maximizing the adiabaticity parameter:

$$Q(t) = \frac{\left(f^2\{\eta(t)\} + g^2\{\eta(t)\}\right)^{3/2}}{\left| f\{\eta(t)\}\dot{g}\{\eta(t)\} - g\{\eta(t)\}\dot{f}\{\eta(t)\} \right|}.$$
(2.31)

with a minimum allowed value such that $Q(t) \geqslant \gamma$ at all times. As the user-defined variable γ is made shorter, the pulse shape does not change, but its profile is stretched into a shorter pulse length τ and the adiabaticity condition is increasingly less well satisfied.

In practice, the desired goals for offset and RF inhomogeneity compensation are determined by the size of the magnetic field, the probe, and the spectroscopic application (e.g., ^{13}C NMR on proteins). The maximum peak and average RF field amplitudes are primarily determined by sample heating restrictions, as well as probe technology. In constructing a numerical pulse, the user sets the path of the adiabatic inversion trajectory in the rotating frame. The length of the pulse τ is made as short as is consistent with adequate inversion performance over the desired bandwidth. For the mixing application discussed here, adequate performance is ultimately judged by how well supercycles of the numerical inversion pulses perform in numerical calculations of magnetization exchange

over the desirable bandwidth. In other words, adequate performance of an adiabatic pulse for single spin inversion is a necessary, but not sufficient, condition for good mixing performance.

In computations of ^{13}C–^{13}C exchange at high magnetic field, this paper pursues the case of pulses with constant RF amplitude. Although an ideal adiabatic inversion trajectory can only be obtained with an infinite frequency sweep when the amplitude is constant, constant-amplitude inversion pulses can perform well in mixing experiments even if this constraint is not strongly obeyed. With numerical optimization, the frequency sweep of a constant amplitude adiabatic inversion pulse is similar to a linear frequency ramp during the middle portion of the pulse. The departure from linearity at the extremes of the pulse is, however, often helpful in maximizing mixing efficiency. Fig. 2 illustrates two pulse envelopes used in some of our ^{13}C–^{13}C exchange experiments at 500 MHz. The frequency sweep shown in dashes is a linear ramp. The numerically derived pulse, calculated based on constant adiabaticity, is also primarily linear, although with a different slope.

As implied by Eq. (2.29), the scaling factor of the J interaction is maximized when the extent of the frequency sweep is limited. This point is made more clear by the specific case of the linear frequency ramp given below. The numerical algorithm guarantees that minimum adiabaticity is achieved at all time points over the whole range of resonance offsets. With a limited frequency sweep, there is always some frequency $\delta_j \in [\delta_{min}, \delta_{max}]$ such that $\delta(t) - \delta_j = 0$ over much of the middle portion of the pulse. The adiabaticity condition is the same at all points over this range, $Q(t) = v_{RF}^2/\dot{\delta}(t) \geqslant \gamma$, which yields a linear frequency sweep, given the imposed constraint of minimum constant adiabaticity. Accordingly, a linear frequency sweep is an excellent model for these numerically derived pulses and indeed linear ramps can perform well experimentally.

2.4. Scaling of the homonuclear J interaction with linear frequency ramps

It is interesting to see how the scaling factor given by Eq. (2.29) behaves in a specific example. Linear frequency ramps are not only a good model for pulses based on constant adiabaticity, but the integral in Eq. (2.29) is amenable to an approximate solution for relatively small resonance offsets δ_j. Here we consider a linear ramp of total width $2\delta_{max}$ with a frequency ramp $\delta(t) = \delta_{max} - kt$ and constant RF amplitude v_{RF}. To make the solution most instructive, we assume that the net effect of the trajectory can be approximated by a single scaling factor α of the chemical shift difference $\Delta\delta$. This approach will yield a scaling factor analogous to Eq. (2.12) where $\Delta\delta_{eff} = \alpha \cdot \Delta\delta$:

$$\lambda = \frac{2}{\Delta\delta_{eff}\tau} \sin\left\{\frac{\Delta\delta_{eff}\tau}{2}\right\}. \tag{2.32}$$

With the definitions

$$\chi(t) = \Delta\delta \int_0^t dt' \frac{\delta(t')}{\sqrt{\delta^2(t') + v_{RF}^2(t')}},$$

$\theta(t) = \Delta\delta \cdot \alpha t$, and $\Delta\delta = \delta_1 - \delta_2$, the cosine term in Eq. (2.29) can be factored as follows:

$$\begin{aligned} \cos\{\chi(t)\} &= \cos\{\Delta\delta \cdot \alpha t + (\chi(t) - \Delta\delta \cdot \alpha t)\} \\ &= \cos\{\Delta\delta \cdot \alpha t\} \cos\{\chi(t) - \Delta\delta \cdot \alpha t\} \\ &\quad - \sin\{\Delta\delta \cdot \alpha t\} \sin\{\chi(t) - \Delta\delta \cdot \alpha t\} \\ &\approx \cos\{\Delta\delta \cdot \alpha t\} - \{\chi(t) - \Delta\delta \cdot \alpha t\} \sin\{\Delta\delta \cdot \alpha t\} \\ &\approx \cos\{\Delta\delta \cdot \alpha t\} - \{\chi(t) - \Delta\delta \cdot \alpha t\} \cdot \{\Delta\delta \cdot \alpha t\}. \end{aligned} \tag{2.33}$$

This approximation holds through $O\{\chi(t) - \Delta\delta \cdot \alpha t\}$. The best analytical solution of the form of the first term involves selection of α such that the second term in Eq. (2.33) is zero. A value that is independent of $\Delta\delta$ is obtained only for small $\Delta\delta$ such that $\Delta\delta \cdot \alpha\tau/2$ is in a small angle. This condition is obeyed sufficiently in the cases considered in this paper. The solution to the problem of optimizing α is straightforward and yields the expression:

$$\begin{aligned} \alpha &= \left\{\left(1 + \frac{v_{RF}^2}{\delta_{max}^2}\right)^{3/2} - \frac{v_{RF}^3}{\delta_{max}^3}\right\} \\ &\quad - \frac{3v_{RF}^2}{2\delta_{max}^2} \ln\left\{\frac{\delta_{max}}{v_{RF}} + \sqrt{1 + \frac{\delta_{max}^2}{v_{RF}^2}}\right\}. \end{aligned} \tag{2.34}$$

Eq. (2.34) predicts that the parameter α is 0.62 for the linear ramp pulse shown in Fig. 1. In Fig. 3b, it is seen that this simple model of chemical shift scaling according to $\Delta\delta \rightarrow \alpha \cdot \Delta\delta$ accounts quantitatively for the scaling factor of a chirp pulse. Further details of the derivation Eq. (2.34) are provided in Appendix A.1. For the similarly shaped numerically derived pulse shown in Fig. 1, the best value of α is 0.55 by empirical fitting to the results from the calculated λ at small $\Delta\delta$, as given by Eq. (2.29), and Fig. 3a also demonstrates the suitability of the scaled chemical shift model in the case of numerically derived pulses.

An alternative expression can also be derived without assuming small $\Delta\delta$ by employing an approximation in which the phase function $\chi(t)$ is presumed linear, i.e., $\alpha \cdot \Delta\delta\tau/2 = \chi(\tau/2)$, leading to the approximate scaling factor:

$$\alpha = \left\{\left(1 + \frac{v_{RF}^2}{\delta_{max}^2}\right)^{1/2} - \left|\frac{v_{RF}}{\delta_{max}}\right|\right\}. \tag{2.35}$$

The slope is taken from the center of the trajectory where $t = \tau/2$, which leads to a simpler expression for α
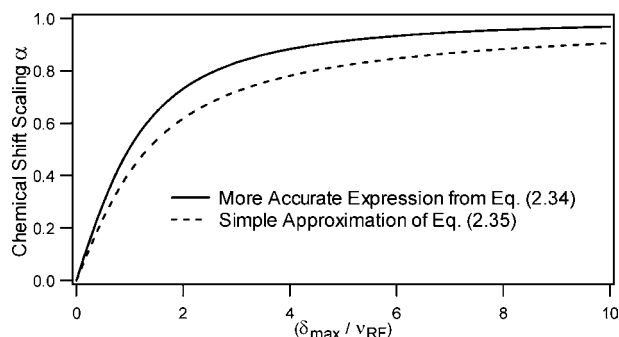
Fig. 4. Chemical shift scaling factors as approximated by the expressions in Eqs. (2.34) and (2.35). The latter offers a more intuitive formulation, but is less accurate. The curves show that $\alpha \approx 0.5$ in the neighborhood $\delta_{max} \approx v_{RF}$ Optimal constant-amplitude sequences have been designed in this study with moderately higher values of δ_{max}, where the pulse is more truly adiabatic.
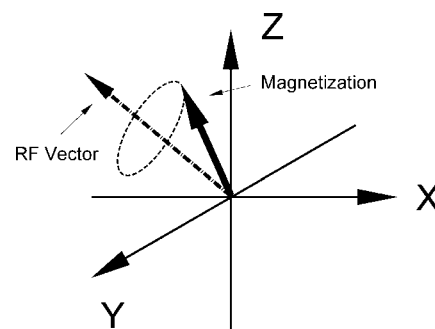

Fig. 5. Vector model of the adiabatic trajectory undertaken by a spin which is influenced by an RF field that is not completely co-parallel initially. In the ideal case, the initial condition of the effective RF field vector in the rotating frame is exactly along the +Z-axis, where the spin polarization begins using an inversion pulse in the setting of longitudinal mixing. However, to make the pulses faster, they begin with a small tilt away from the +Z-axis in this study. The component of spin polarization which is not initially parallel to the effective RF field vector then precesses about the RF field as it is itself changing direction on a much slower time scale. The spin polarization ends up closest to −Z if the net precession angle about the tilting RF field is an odd multiple of π over the total pulse length τ.

than Eq. (2.34) but an underestimate of the degree of chemical shift scaling by about 20%. Fig. 4 shows how the scaling factor α behaves as a function of δ_{max}/v_{RF} via Eqs. (2.34) and (2.35).

Interestingly, although an excellent adiabatic inversion pulse with large δ_{max}/v_{RF} may have a correspondingly large bandwidth, Fig. 4 illustrates that there is little chemical shift scaling under these conditions. Accordingly, a poor λ is obtained in this limit. Interestingly, the chemical shifts are scaled by 0.5 when $\delta_{max} \approx v_{RF}$. The pulse, however, is unlikely to obey the adiabaticity constraint or yield broadbanded inversion unless $\delta_{max} \gg v_{RF}$. In practice, a compromise exists in selecting the optimal δ_{max} since λ becomes larger as $\delta_{max} \to v_{RF}$, while the bandwidth increases with increasing δ_{max} and, in general, the pulse length τ. Although the specific example of a chirp pulse is discussed here, this behavior is fairly general for adiabatic pulses. As v_{RF} decreases or δ_{max} increases, the scaling properties are likely to degrade. A corollary is that exchange slows down in principle as the RF field decreases, and therefore RF field inhomogeneity is expected to degrade the performance of adiabatic sequences to some extent even when each spin is still being perfectly inverted. Of course, the recovered J interaction also decreases at low RF fields in a similar way using composite pulse approaches [5].

2.5. Constraints on the pulse length with finite frequency sweeps

With a finite frequency sweep, the RF field vector does not begin strictly parallel to the longitudinal coherence to be inverted. Consequently, there is a significant component that precesses about the tilting RF field instead of following it in an adiabatic fashion. Fig. 5 illustrates this behavior. The goal of best inversion is accomplished when the component of magnetization that is not locked along the RF field precesses about an angle $n\pi$, where n is odd. At angles $n\pi$ with n even, the

worst inversion properties are expected. This behavior can be appreciated by considering the geometry in Fig. 5. The magnetization begins initially along the Z-axis, and the RF field vector begins at some small angle away from it. Following an adiabatic trajectory, the magnetization precesses around the RF field as it moves from near alignment along +Z to −Z. The magnetization finishes closest to the −Z-axis when there is net π rotation about the RF field axis. This type of "ripple" behavior, i.e., oscillating inversion efficiency with respect to increasing pulse length, is a general feature of semi-adiabatic pulses [42] and is particularly prominent with constant amplitude pulses [21].

In order to ascertain which pulse lengths optimize the inversion efficiency in a finite frequency sweep, the total angle of precession can be computed analytically for the case of a linear ramp pulse:

$$\Omega = \int_0^\tau dt \sqrt{\delta^2(t) + v_{RF}^2}$$
$$= \left\{ \frac{1}{2}\sqrt{\delta_{max}^2 + v_{RF}^2} + \frac{v_{RF}^2}{\delta_{max}} \ln\left[\frac{\delta_{max}}{v_{RF}} + \sqrt{1 + \frac{\delta_{max}^2}{v_{RF}^2}} \right] \right\} \cdot \tau.$$
(2.36)

The pulse length τ is then constrained to be roughly such that Ω is an odd multiple of π. Unfortunately, the adiabaticity criterion is generally violated when $\Omega = \pi$ for the pulses studied here, and consequently we find that both linear ramp pulses and numerically optimized pulses work best in our study in the neighborhood of $\Omega \approx 3\pi$. For instance, in the example discussed above and illustrated in Fig. 2, i.e., a 22 kHz sweep at 7.7 kHz RF field, the optimal pulse via Eq. (2.36) is 153 μs.
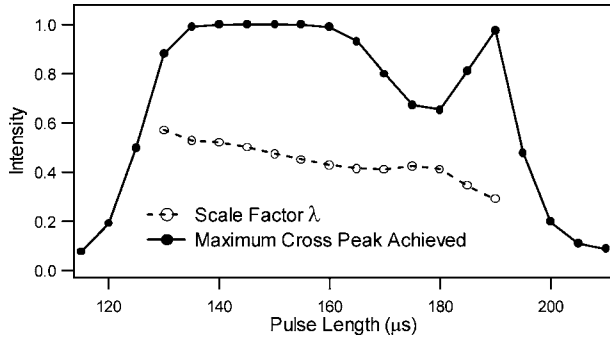
Fig. 6. Pulse length constraints on efficient mixing between two spins. For the system discussed here, the region where the adiabatic pulse length is about 135–160 μs yields maximal exchange because the net precession angle of the spin polarizations is about 3π. Although the interval is fairly broad, mixing not only slows down, but also fails altogether, outside this region. This calculation applies to two spins separated by $\Delta\delta = 7.0$ kHz with an applied RF field of 7.7 kHz. The scaling factor λ is seen to decrease as the pulse length is increased. This behavior corresponds to the reduction in the scaling factor seen with lower pulsing rates.

In fact, a mixing bandwidth of at least 7 kHz is obtained even when the pulse length is as short as 135 μs, so this timing constraint is not very restrictive in practice. Fig. 6 illustrates the maximum cross-peak obtained in an exact two spin calculation when $\Delta\delta = 7$ kHz. It shows a broad interval from 135 to 160 μs where the pulse length is acceptable. The figure also illustrates that the scaling factor λ falls as the pulse length increases, so it is helpful to keep the pulse as short as possible. On the other hand, a longer pulse yields better tolerance to RF inhomogeneity because in that case the sequence continues to perform efficiently at lower RF powers than the nominal value. This behavior occurs because a longer τ is needed to make $\Omega \approx 3\pi$ as ν_{RF} is reduced. Similar considerations apply to numerically optimized pulses derived from finite frequency sweeps.

The constraints on the pulse length result from the limited extent of the sweep using constant RF power. This may be a disadvantage of constant amplitude pulses under some conditions. However, the use of RF amplitude envelopes at the edges of the pulse, as generally applied in adiabatic pulses, generally reduces the scaling factor λ as derived in Section 2.2. For the applications of interest here, the time restrictions have proven reasonable.

2.6. Further treatment of finite pulse effects

The transverse terms in Eq. (2.24) lead to small additional rotations of the coupling. These could degrade mixing performance and must be removed by some supercycling approach. The MLEV [4] and other supercycling approaches [35] are highly efficient in both composite pulse and adiabatic decoupling [43], as well as

mixing. In a general way, the error terms contribute to the toggling frame Hamiltonian as follows:

$$\tilde{H}_0(t) = \left\{ \delta_1 \cos\theta(t)I_{z1} + \bar{\alpha}(t)I_{x1} + \bar{\beta}(t)I_{y1} + \bar{\gamma}(t)I_{z1} \right\}$$
$$+ \left\{ \delta_2 \cos\theta(t)I_{z2} + \bar{\alpha}(t)I_{x2} + \bar{\beta}(t)I_{y2} + \bar{\gamma}(t)I_{z2} \right\}$$
$$+ J\vec{I}_1 \cdot \vec{I}_2, \tag{2.37}$$

where the vector $\left\{ \bar{\alpha}(t), \bar{\beta}(t), \bar{\gamma}(t) \right\}$ defines a small error rotation. Without loss of generality, the $\bar{\gamma}(t)I_{zj}$ term is included in the predominant rotations defined by $\delta_j \cos\theta(t)I_{zj}$. In particular, the phase factor $\chi(t)$ of Eq. (2.27) can be redefined to include this term:

$$\chi'(t) = \int_0^t dt'(\delta_1 - \delta_2)\cos\theta(t') + \int_0^t dt'\left\{\bar{\gamma}_1(t') - \bar{\gamma}_2(t')\right\}. \tag{2.38}$$

Supercycling eliminates the single spin contributions to the Hamiltonian in the context of a train of inversion pulses [4,35,36], and this problem is not considered further here. Instead, the impact of the error rotations on the form of the coupling is pursued further. To examine the effect of the errors through first order, it is helpful to define the phase accumulated by each of the error rotations:

$$\alpha(t) = \int_0^t dt' \bar{\alpha}(t'),$$
$$\beta(t) = \int_0^t dt' \bar{\beta}(t'), \tag{2.39}$$
$$\gamma(t) = \int_0^t dt' \bar{\gamma}(t').$$

Toggling frames can be defined in terms of these phase factors. Approximations for the effects of the rotations are included through linear order in the phase factors:

$$I_{xj} \approx I_{xj}\cos\beta_j(t) - I_{zj}\sin\beta_j(t),$$
$$I_{yj} \approx I_{yj}\cos\alpha_j(t) + I_{zj}\sin\alpha_j(t),$$
$$I_{zj} \approx I_{xj}\sin\beta_j(t) - I_{yj}\sin\alpha_j(t)\cos\beta_j(t) \tag{2.40}$$
$$+ I_{zj}\cos\alpha_j(t)\cos\beta_j(t).$$

These approximations involve sequential transformations about each angle, i.e., the first order Baker's–Hausforf–Campbell expansion [44], which preserves the unitarity of rotations.

In the second toggling frame [39], the error rotations contribute single-, zero-, and double-quantum terms to the J-coupling Hamiltonian [15]. The Hamiltonian can be expressed in the second toggling frame via a primary rotation about $\chi(t)$, as described by Eqs. (2.8)–(2.10), followed by the transformations described by Eq. (2.38). The overall coupling Hamiltonian in the second toggling frame can be then written as follows:

$$\tilde{H}_1(t) = J\big\{\cos\chi'(t)\cos\beta_1(t)\cos\beta_2(t)$$
$$+ \sin\beta_1(t)\sin\beta_2(t)\big\}I_{x1}I_{x2}$$
$$+ J\big\{-\sin\chi'(t)\cos\beta_1(t)\cos\alpha_2(t)$$
$$- \sin\beta_1(t)\sin\alpha_2(t)\cos\beta_2(t)\big\}I_{x1}I_{y2}$$
$$+ J\big\{-\cos\chi'(t)\cos\beta_1(t)\sin\beta_2(t)$$
$$- \sin\chi'(t)\cos\beta_1(t)\sin\alpha_2(t)$$
$$+ \sin\beta_1(t)\cos\alpha_2(t)\cos\beta_2(t)\big\}I_{x1}I_{z2}$$
$$+ J\big\{\sin\chi'(t)\cos\alpha_1(t)\cos\beta_2(t)$$
$$- \sin\alpha_1(t)\cos\beta_1(t)\sin\beta_2(t)\big\}I_{y1}I_{x2}$$
$$+ J\big\{\cos\chi'(t)\cos\alpha_1(t)\cos\alpha_2(t)$$
$$+ \sin\alpha_1(t)\cos\beta_1(t)\sin\alpha_2(t)\cos\beta_2(t)\big\}I_{y1}I_{y2}$$
$$+ J\big\{\cos\chi'(t)\cos\alpha_1(t)\sin\alpha_2(t)$$
$$- \sin\chi'(t)\cos\alpha_1(t)\sin\beta_2(t)$$
$$- \sin\alpha_1(t)\cos\beta_1(t)\cos\alpha_2(t)\cos\beta_2(t)\big\}I_{y1}I_{z2}$$
$$+ J\big\{-\cos\chi'(t)\sin\beta_1(t)\cos\beta_2(t)\sin\chi'(t)$$
$$\times \sin\alpha_1(t)\cos\beta_2(t)$$
$$+ \cos\alpha_1(t)\cos\beta_1(t)\cos\beta_2(t)\big\}I_{z1}I_{x2}$$
$$+ J\big\{\cos\chi'(t)\sin\alpha_1(t)\cos\alpha_2(t)$$
$$+ \sin\chi'(t)\sin\beta_1(t)\cos\alpha_2(t)$$
$$- \cos\alpha_1(t)\cos\beta_1(t)\sin\alpha_2(t)\cos\beta_2(t)\big\}I_{z1}I_{y2}$$
$$+ J\big\{+\cos\chi'(t)[\sin\beta_1(t)\sin\beta_2(t)$$
$$+ \sin\alpha_1(t)\sin\alpha_2(t)]$$
$$+ \sin\chi'(t)[\sin\beta_1(t)\cos\alpha_2(t)$$
$$- \cos\alpha_1(t)\sin\beta_2(t)]$$
$$+ \cos\alpha_1(t)\cos\beta_1(t)\cos\alpha_2(t)\cos\beta_2(t)\big\}I_{z1}I_{z2}.$$
$$(2.41)$$

Fortunately, most of these terms vanish during the sequence when supercycling is applied. The net rotation due to an adiabatic inversion pulse of phase X is the following in the most general case:

$$U_{RF} = \exp\big\{-i\pi[(I_{x1}+I_{x2})\cos\varepsilon + (I_{y1}+I_{y2})\sin\varepsilon]\big\}$$
$$\times \exp\{-i\varphi(I_{z1}+I_{z2})\}. \qquad (2.42)$$

This expression follows from the assumption of inversion of longitudinal coherences: $I_{zj} \rightarrow -I_{zj}$, which in turn results from the definition of an adiabatic inversion pulse. However, the net rotation imposed by the pulses applied here is very close to that of a typical π pulse:

$$U_{RF} = \exp\{-i\pi(I_{x1}+I_{x2})\}. \qquad (2.43)$$

As discussed in Section 2.5, the net precession angle about the adiabatic trajectory is 3π for the pulses discussed here, and as a result the overall rotations yield $X \rightarrow X, Y \rightarrow -Y, Z \rightarrow -Z$, as summarized by Eq. (2.43). For simplicity the main features of supercycling are

discussed in the context of pulses which approximately obey Eq. (2.43).

Pairs of inversion pulses with the same phase, i.e., XX, cancel out bilinear terms of the form $I_{xi}I_{yj}$ and $I_{xi}I_{zj}$. An example is given here

$$\exp\{-i\pi(I_{x1}+I_{x2})\}\exp\{-icI_{x1}I_{z2}\}$$
$$\times \exp\{-i\pi(I_{x1}+I_{x2})\}\exp\{-icI_{x1}I_{z2}\}$$
$$= \exp\{-i2\pi(I_{x1}+I_{x2})\}$$
$$\times \exp\approx\{+icI_{x1}I_{z2}\}\exp\{-icI_{x1}I_{z2}\}$$
$$\approx \exp\{-i2\pi(I_{x1}+I_{x2})\}, \qquad (2.44)$$

where c is the amplitude of the bilinear term and is assumed to be small in order to recombine the rotations. Phase inversion, i.e., $X\bar{X}$, is used in order to cancel terms of the form $I_{yi}I_{zj}$. In this case, application of an inverse phase pulse reverses the sign of the coefficient $c \rightarrow -c$, while the inversion of the X pulse does not affect the bilinear term directly

$$\exp\{+i\pi(I_{x1}+I_{x2})\}\exp\{-i(-c)I_{y1}I_{z2}\}$$
$$\times \exp\{-i\pi(I_{x1}+I_{x2})\}\exp\{-icI_{y1}I_{z2}\}$$
$$= \exp\{-icI_{x1}I_{z2}\}\exp\{-icI_{x1}I_{z2}\} \approx 1, \qquad (2.45)$$

Terms of the form $I_{xi}I_{zj}$ are eliminated by either XX or $X\bar{X}$.

With elimination of all off-diagonal terms, the Hamiltonian simplifies to the form:

$$\tilde{\tilde{H}}_1(t) = J\big\{\cos\chi'(t)\cos\beta_1(t)\cos\beta_2(t)$$
$$+ \sin\beta_1(t)\sin\beta_2(t)\big\}I_{x1}I_{x2}$$
$$+ J\big\{\cos\chi'(t)\cos\alpha_1(t)\cos\alpha_2(t)$$
$$+ \sin\alpha_1(t)\cos\beta_1(t)\sin\alpha_2(t)\cos\beta_2(t)\big\}I_{y1}I_{y2}$$
$$+ J\big\{\cos\alpha_1(t)\cos\alpha_2(t)\cos\beta_1(t)\cos\beta_2(t)$$
$$+ \cos\chi'(t)[\sin\beta_1(t)\sin\beta_2(t) + \sin\alpha_1(t)\sin\alpha_2(t)]$$
$$+ \sin\chi'(t)[\sin\beta_1(t)\sin\alpha_2(t)$$
$$- \sin\alpha_1(t)\sin\beta_2(t)]\big\}I_{z1}I_{z2}. \qquad (2.46)$$

To some degree, the error terms seen in Eq. (2.46) reduce the attenuation of the terms involving transverse spin operators at large chemical shift differences. Fig. 3 illustrates this effect by comparison exact spin calculations with the approximations given by Eqs. (2.27)–(2.29). Via the error rotations there is also some scaling of the $I_{z1}I_{z2}$ term.

The Hamiltonian of Eq. (2.44) is a linear combination of $I_{x1}I_{x2}$ and $I_{y1}I_{y2}$, which in general contains both zero-quantum and double-quantum components when these terms are not equal. For spin exchange, only the zero-quantum component is desired. Double-quantum contamination results in loss of signal. The double-quantum component can be eliminated by cycling with alternating sets of X and Y phase pulses, which averages the coupling in the X and Y directions [36]:

$$\tilde{\tilde{H}}_1(t) = \frac{1}{2}J\Big\{\cos\chi'(t)(\cos\beta_1(t)\cos\beta_2(t)$$
$$+ \cos\alpha_1(t)\cos\alpha_2(t)) + (\sin\beta_1(t)\sin\beta_2(t)$$
$$+ \sin\alpha_1(t)\cos\beta_1(t)\sin\alpha_2(t)\cos\beta_2(t))\Big\}$$
$$\cdot\big[I_{x1}I_{x2} + I_{y1}I_{y2}\big]$$
$$+ J\Big\{\cos\alpha_1(t)\cos\alpha_2(t)\cos\beta_1(t)\cos\beta_2(t)$$
$$+ \cos\chi'(t)\big[\sin\beta_1(t)\sin\beta_2(t)$$
$$+ \sin\alpha_1(t)\sin\alpha_2(t)\big]$$
$$+ \sin\chi'(t)\big[\sin\beta_1(t)\sin\alpha_2(t)$$
$$- \sin\alpha_1(t)\sin\beta_2(t)\big]\Big\}I_{z1}I_{z2}. \qquad (2.47)$$

Recall that the second term is a pure flip–flop (zero quantum) Hamiltonian, as revealed by the expression:

$$\{I_{x1}I_{x2} + I_{y1}I_{y2}\} = 1/2\{I_{+1}I_{-2} + I_{-1}I_{+2}\}. \qquad (2.48)$$

The derivations explicitly discussed here apply to small error angles, but in practice the efficiency of supercycling schemes for producing a pure zero-quantum Hamiltonian is not so restrictive. However, regardless of the specific form of the toggling frame Hamiltonian, it is clear that trains of X and $\bar{X}$ pulses alone are insufficient to eliminate double-quantum contamination.

In practice it is helpful to augment the MLEV scheme with additional supercycling [35]. The P5 phase alternation scheme has been particularly successful for mixing and decoupling applications with adiabatic pulses [22,26,27,45], and it also improves the performance of suitable optimized constant-amplitude pulses as presented below. One variation of this scheme is P5M4, which involves MLEV cycling of the P5 element, given by $P5 = \{0°, 150°, 60°, 150°, 0°\}$. Because one P5 cycle of inversion pulses is itself essentially a composite inversion pulse, MLEV cycling is still applicable to both the elimination of single spin rotation errors and their explicit effects on the spin coupling as outlined above. The desirability of additional XY cycling also remains applicable in these more complicated supercycling schemes because double-quantum contamination is not eliminated by P5/MLEV approaches. In general, very good mixing sequences can be generated without additional P5 cycling; however, in practice slightly shorter adiabatic pulses with improved scaling factors can be obtained using the P5M4 approach, where the P5 unit is cycled according to MLEV-4 as follows: $XX\bar{X}\bar{X}$.

3. Development and simulation

It is at high field where adiabatic approaches have the most potential utility for improving mixing efficiency relative to composite pulse sequences. Two commonly employed composite pulse sequences are the DIPSI [15,16] and FLOPSY [18] schemes. The major advantage of the DIPSI sequences is that they are suitable for isotropic mixing over relatively small bandwidths, whereas the FLOPSY approach was designed primarily for longitudinal exchange among spins. However, the simulations given by Peti et al. confirmed that FLOPSY sequences have much greater bandwidth and better J scaling properties than the DIPSI sequences [27]. Like FLOPSY, the approach of mixing via trains of adiabatic inversion pulses described here has been developed for the case of longitudinal exchange. Because the FLOPSY-16 sequence has the best bandwidth and J scaling properties among commonly employed sequences, it is the most appropriate benchmark for comparison with new adiabatic sequences.

In our experiments we are particularly interested in optimizing ^{13}C–^{13}C exchange for sidechain assignments in proteins at high magnetic fields. For ^{13}C in proteins, the maximum chemical shift dispersion is approximately 60 ppm [1], which corresponds to 8 kHz at 500 MHz magnetic field. However, the maximum chemical shift difference between neighboring ^{13}C spins corresponds only to about 53 ppm, i.e., 7 kHz at 500 MHz. For ^{13}C mixing experiments, we routinely employ a constant RF field strength of 7.7 kHz (i.e., a π pulse length of 64.94 μs) in our experiments at 500, 600, and 750 MHz field strengths. The numerical adiabatic pulse given as an example in Fig. 2 was computed via the algorithm of Rosenfeld et al. with a total frequency sweep of 25 kHz. That pulse provides a nominal 8 kHz frequency bandwidth. These parameters are appropriate for the case of a 500 MHz spectrometer. The resulting pulse was 151 μs in length, obtained by minimizing the pulse timing while retaining adequate adiabaticity. The numerically calculated scaling factor for the J-coupling, shown earlier in Fig. 3, illustrated how the effective J interaction decreases with increasing resonance offsets, and it compared the exact two spin behavior with the analytical treatments developed in the preceeding theoretical section. Similar results were obtained using a linear ramp pulse, which can be treated analytically for the case of relatively small $\Delta\delta$. Over the bandwidth appropriate for 500 MHz, i.e., 7–8 kHz, the analytical results illustrated in Fig. 3 proved quantitatively accurate, while increasing divergence in the analytical theory is obtained at higher offsets. In general, the scaling factor λ decreases more slowly than predicted by Eq. (2.29) because of terms which are independent of $\Delta\delta$, as seen in Eq. (2.47) when additional finite pulse effects are considered.

In practical applications, it is particularly in the high field regime above 500 MHz where adiabatic approaches have the most potential utility for improving the efficiency of mixing experiments relative to the FLOPSY-16 sequence. At 750 MHz, for example, the total aliphatic bandwidth is slightly less than 12 kHz as a maximal range, while the largest expected shift differences are approximately 10.5 kHz. Fig. 7 shows two frequency sweeps
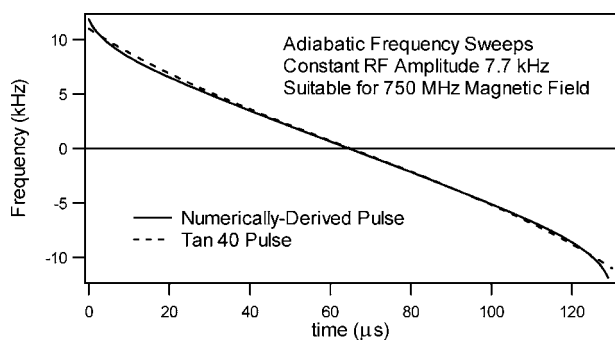
Fig. 7. Modified frequency sweeps for use at 750 MHz. The numerically derived pulse is qualitatively similar to the pulse developed for application at 500 MHz. The optimal tan 40 pulse is also shown as a dashed line. It is in fact almost linear, but is more efficient than linear ramp pulses experimentally and in simulations.

which are applicable at 750 MHz. The numerically shaped pulse involves a total 22 kHz sweep at a constant RF field amplitude of 7.7 kHz. The pulse was calculated to cover a 12 kHz frequency bandwidth of spin resonance offsets. Using the augmented phase cycle P5M4 [43] with XY alternation, the pulse length could be made as short as 130 µs with good performance. Within the relevant bandwidth of $\delta_j = \pm 6$ kHz, Fig. 8 shows a contour plot which compares the cross-peak intensities given by FLOPSY-16 and the numerically derived adiabatic pulse
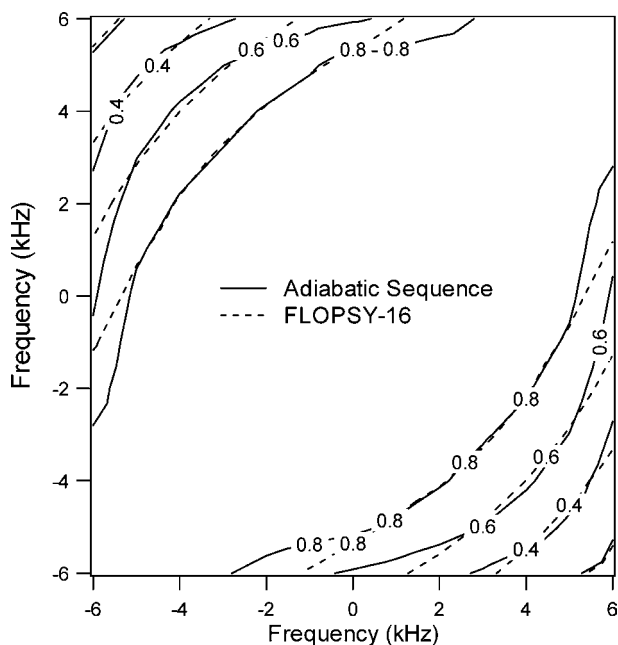
Fig. 8. Contour plot of the cross-peak intensity obtained in a two spin system as a function of the spin frequencies. The adiabatic sequence based on the pulse shown in Fig. 7 is compared to FLOPSY-16 at 15.5 ms mixing time. Increased efficiency is seen along the "anti-diagonal" where $\delta_1 = -\delta_2$. At the edges, the adiabatic pulse was not designed to perform as efficiently, as almost no spins are found in those regions at 750 MHz.

shown in Fig. 7. In this case, the numerical adiabatic pulse was applied with the slightly shorter pulse length of 129 µs in order to enable sampling of the calculations at the same mixing time as FLOPSY-16 at 15.5 ms. For relatively large values of $\Delta\delta$, where the efficiency of spin exchange is most markedly reduced, the contour plot shows that the adiabatic sequence has slightly greater bandwidth. At the edges, however, there is decreasing performance near the limits of where the pulse is constructed to behave adiabatically, i.e., $\delta_j = \pm 6$ kHz. All simulations were performed using programs written by the authors which were optimized for homonuclear systems of two or three spins. For more convenient implementation, we have pursued the possibility of applying an analytical pulse shape which would emulate the shapes of the numerically derived pulses. The shapes of the calculated pulses, as seen in Figs. 2 and 7, are qualitatively similar to truncated tangent functions with constant amplitude [32]. Accordingly we optimized a frequency sweep of the form:

$$\delta(t) = -A \tan\left\{\varepsilon\left(t - \frac{\tau}{2}\right)\right\}. \qquad (3.1)$$

The initial angle of the tangent is given by $\Theta = \varepsilon\tau/2$, and for our applications at 600 and 750 MHz, the best results have been obtained in the neighborhood $\Theta = 40°$ in simulations. Here this pulse is designated a "tan 40" pulse. To accommodate the required sweep width, the parameter A is adjusted such that $\delta_{max} = A \tan\{\varepsilon\tau/2\}$. The tan 40 pulse applied experimentally is also illustrated in Fig. 7.

The theoretical results of Section 2 are quite valuable in sequence design. However, in addition to the need to evaluate sequences at larger values of $\Delta\delta$ where the small angle approximations become less accurate, the influences of phase cycling and finite pulse effects are difficult to quantify by analytical approximations alone. Accordingly, we have tested candidate sequences using exact calculations of exchange in two and three spin systems. Fig. 9 demonstrates the evolution of exchange
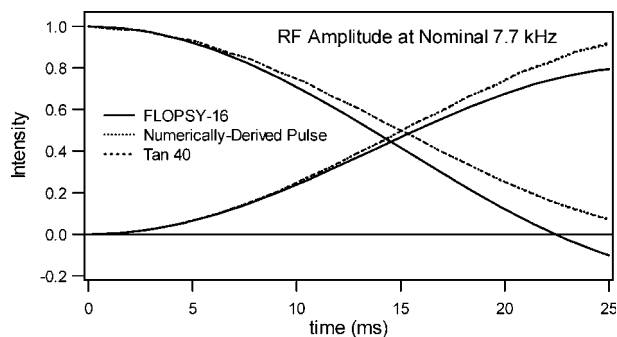

Fig. 9. Two spin simulation with $\Delta\delta = 10.5$ kHz which is appropriate for a typical threonine Cβ–Cγ peak separation in a protein at 750 MHz. The cross-peak obtained with FLOPSY-16 is reduced especially at longer mixing times where double-quantum decay becomes significant. The tan 40 pulse gives almost identical performance to the numerically derived pulse.
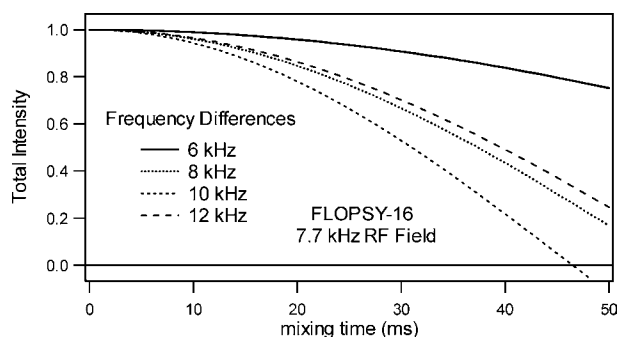
Fig. 10. Decay of total spin polarization in a two spin system during the FLOPSY-16 pulse sequence. Above the RF field of 7.7 kHz, the degree of double-quantum contamination in the effective Hamiltonian seen here becomes increasingly marked and later oscillatory.
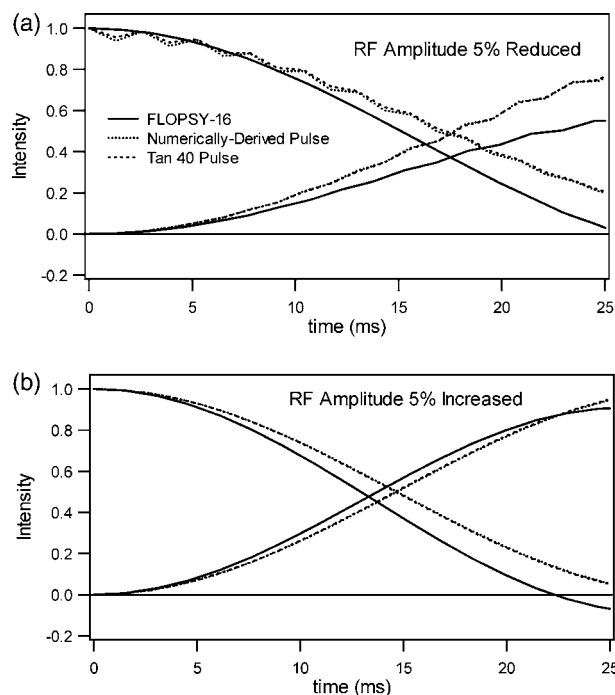

Fig. 11. Two spin simulations illustrating the effect of RF inhomogeneity on a two spin system which is otherwise like the one shown in Fig. 9. At an RF field which is lower than nominal, as seen in part (a), the numerically derived and tan 40 pulses maintain improved mixing efficiency. It appears that the double-quantum decay property obtained with FLOPSY-16 is worse at lower RF fields. In contrast, the rate of mixing with FLOPSY-16 increases more rapidly so that at higher than nominal RF fields there is faster mixing using the composite pulse FLOPSY-16 sequence.

between two spins with $\Delta\delta = 10.5$ kHz using the pulses shown in Fig. 7. (In the simulations, note that the curves for the tan 40 and numerically derived pulses are almost indistinguishable in most cases.) As reflected in the contour plot in Fig. 8, exchange is only slightly faster at shorter mixing times <15 ms. However, at longer times, the adiabatic sequences attain higher intensities. This behavior results from the fact that the FLOPSY sequences retain an effective double-quantum contaminant which attenuates total polarization at larger resonance offsets. Fig. 10 illustrates this decay behavior, which rapidly accumulates when $\Delta\delta \geqslant \nu_{RF}$. At higher values of $\Delta\delta$, the degree of double-quantum decay becomes large and oscillatory. In contrast, there is essentially no significant loss of total signal in spin simulations of the adiabatic sequences, which are compensated with respect to double-quantum contamination via XY cycling of the entire phase alternation scheme.

Another important consideration is the effect of RF inhomogeneity, which is approximately ±7.5% in the probes employed in this laboratory. Fig. 11 illustrates how the adiabatic sequences compare to FLOPSY in the presence of uncertainty about the RF field strength. At low RF power, i.e., 5% below the nominal value, the advantage of the adiabatic sequences over FLOPSY is increased, although both types of sequences exhibit slower exchange rates. The tendency of FLOPSY to lose total signal is predicted to increase under these conditions as well. On the other hand, at higher RF power, i.e., 5% above the nominal field, exchange via FLOPSY increases more rapidly than that obtained with the adiabatic sequences, and FLOPSY exchange becomes moderately faster. In practice, the results seen experimentally are expected to reflect a complex weighted average over the RF inhomogeneity, as determined by the coil and sample geometries.

In the assignment of protein sidechains, the only pure two spin systems are the Cα–Cβ pairs in alanine, aspartic acid, asparagine, and serine. The Cα–Cβ pairs in the aromatic amino acids can also be viewed as homonuclear two spin systems, barring leakage of magnetizations into the aromatic rings, which is a fairly small effect for these sequences. The most challenging two spin pair is alanine, where $\Delta\delta \approx 6.5$ kHz at 750 MHz. In all of the other amino acids, the influence of multiple spin dynamics is expected to dominate cross-peak intensities. The simplest example is the three spin system seen in threonine, glutamine, and glutamic acid. In multiple spin systems, it is not always possible to obtain complete exchange of polarization from one spin to another; instead, there is a ceiling on the maximum exchange peak [5], which may be difficult to calculate, and it depends on the effective spin Hamiltonian. Fig. 12 illustrates how the adiabatic and FLOPSY sequences are expected to behave in a typical threonine residue, beginning with Cα polarization for illustration. Here parameters which are appropriate for the Threonine-16 residue in the SH3 domain of CD2BP1 [46] are applied. The threonine Cβ–Cγ spin pair is the largest chemical shift difference found among the aliphatic ^{13}C resonances in proteins, with typical values $\Delta\delta \approx 9$ kHz. The Cα, Cβ, and Cγ frequencies of Threonine-16 are 2.9, 4.6, and −4.5 kHz, respectively, when the carrier is set to 43 ppm, as typi-
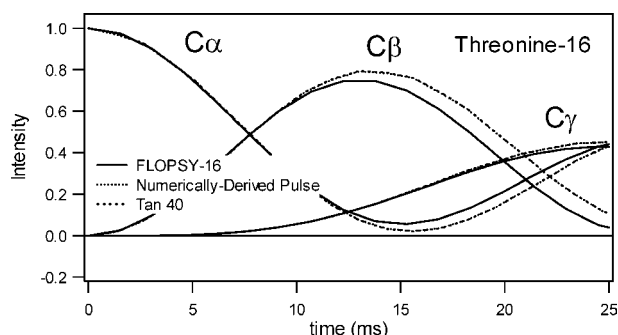
Fig. 12. Three spin simulation illustrating the anticipated behavior of mixing, beginning with Cα polarization, using parameters appropriate for the Thr-16 residue of the SH3 domain of CD2BP1. Of note, slower two spin exchange maps to incomplete mixing at long mixing times across the difficult spin pair of Cβ–Cγ, which is an effect of multiple spin dynamics.

cally implemented in mixing experiments. An interesting feature of the exchange process is that the slower transfer seen in FLOPSY-16 between the Cβ and Cγ nuclei maps to a reduced maximum cross-peak intensity at long mixing times in the three spin case. Therefore, although the FLOPSY and adiabatic sequences are expected to behave very similarly when the resonance offsets are small, it is expected that significant improvements should be seen in cases like threonine where exchange is fairly slow and maximum cross-peak intensities are limited by the slow Cβ–Cγ exchange process.

4. Results

The main application discussed in this paper is HCCH–TOCSY, which is usually implemented as a three-dimensional experiment, as reviewed in the monograph of Cavanaugh et al. [1]. However, to explore various conditions efficiently, we have acquired two-dimensional ^{1}H–^{1}H spectra, where the cross-peaks were obtained via ^{13}C–^{13}C TOCSY applied to relayed coherences from the observed ^{1}H nuclei. The application of a simple adiabatic sequences is shown in Fig. 13. The protein is the 7 kDa SH3 domain from the CD2-related signaling protein CD2BP1 [46]. Fig. 13a illustrates the ^{1}H–^{1}H spectrum obtained via ^{13}C–^{13}C exchange. The larger boxes (region A in the left upper, region B in the right lower) are defined for the purpose of examining regional integrals. This spectrum was acquired using the numerically defined adiabatic pulse shown in Fig. 1 with alternation of the pulse phases according to both MLEV-16 and XY cycling. Performed on a Bruker 500 MHz spectrometer using a recently introduced Bruker cryoprobe, the nominal RF field strength was 7.7 kHz. Although the exchange dynamics under study here are the same in two- and three-dimensional versions
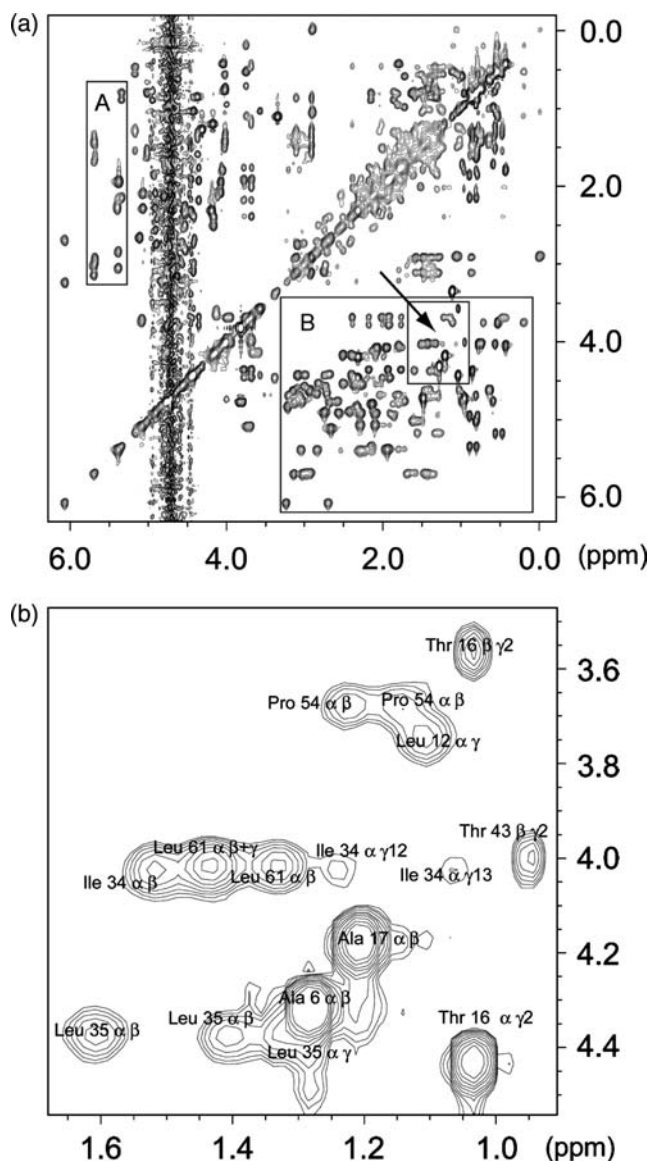

Fig. 13. Two dimensional ^{1}H–^{1}H spectrum of the SH3 Domain of CD2BP1 obtained using a mixing sequence based on the numerically derived pulse shown in Fig. 2. This spectrum was obtained via exchange among ^{13}C spins, although their directly bonded aliphatic protons are detected, as shown here. In part (a), two regions, A and B, are defined in order to investigate integrals over many spin exchange processes. The smaller region shown in the right lower quadrant, and indicated by an arrow, is expanded in part (b). Here the peaks assignments are shown. Most of these are overlapping, but both Thr-16 cross-peaks are isolated and available for integration. The Ala-27 peak (now shown) is also cleanly isolated. The experiment was performed at 500 MHz on a Bruker 500 outfitted with a Bruker cryogenic probe. This probe is useful because it increases the sensitivity of NMR experiments by approximately three-fold. The RF field was 7.7 kHz, a fairly typical value for this application.

of the HCCH–TOCSY experiment, the 2D planes exhibit extensive spectral overlap among different ^{1}H nuclei, as seen in Fig. 13b, where the resonance assignments are labeled explicitly. However, the Cα–Cβ and Cα–Cγ cross-peaks of Threonine-16 are isolated

and can be cleanly integrated. In a similar way, the Cα–Cβ peak of Alanine-27 is spectrally isolated (not shown in Fig. 13b) and is suitable for quantitative study of the exchange dynamics.

The backbone and sidechain chemical shifts of the SH3/CD2BP1 module were obtained via standard backbone chemical shift experiments (HNCA, HNCOCA, HNCACB, and HNCOCACB) performed on a Bruker 500 MHz spectrometer [1]. The sidechain assignments were obtained via a three-dimensional HCCH–TOCSY spectrum acquired on Bruker 600 MHz machine. The SH3 domain was expressed as a thrombin cleaveable GST fusion protein using a construct based on the pGEX-4T-1 vector (Pharmacia). The plasmid construct was provided by our collaborators Jing Li, Ellis Reinherz, and co-workers [46]. Isotope-enriched M9 medium was used in order to make ^{13}C, ^{15}N-labeled protein, and the product was purified by cleaving the SH3 domain from the GST fusion partner after annealing the fusion protein to GST resin. In addition to removal of thrombin by benzamidine resin, further purification via gel filtration chromatography was found necessary to stabilize the sample with respect to proteolysis. The NMR experiments were performed with a 250 μL sample in a Shigemi NMR tube at 0.64 mM final protein concentration in a 18 mM phosphate buffer at pH 6.7 with 130 mM NaCl and 10% D_2O for magnet locking. The sample has shown >90% stability after six months if trace quantities of protease inhibitors are included in the final buffer.

Experimentally, in addition to their role as a model system, it was found that simple linear ramp pulses perform fairly well in ^{13}C–^{13}C exchange experiments at 600 MHz but are moderately less efficient than the more carefully optimized pulse sequences also presented here by approximately 10–20%. Still, we found it instructive to explore mixing behavior with respect to the frequency sweep and pulse length in HCCH–TOCSY experiments. Experimentally, significant signal losses were observed following application of the mixing cycle outside the neighborhood of $\delta_{max} \approx 11$ to 12 kHz and $\tau \approx 130$ to 150 μs. Fig. 14 illustrates the dependence of the Threonine-16 cross-peaks acquired using a Bruker 600 spectrometer outfitted with a triple resonance probe made by Nalorac as the pulse parameters are varied. In this plot and in Figs. 15 and 16 below, the intensities of the Cα–Cγ and Cβ–Cγ peaks are added together in order to assess the total transfer from Cβ to Cγ, which is rate-limiting. The best results were obtained with $\delta_{max} \approx 11$ kHz. As the pulse length τ is increased, better performance is expected at points of lower RF power in the sample coil while exchange slows down at points near the nominal RF field strength, according to the analytical theory of Section 2. Here the optimal point is obtained at approximately $\tau \approx 140$ μs. In these experiments, a total of 144 pulses was applied to complete a
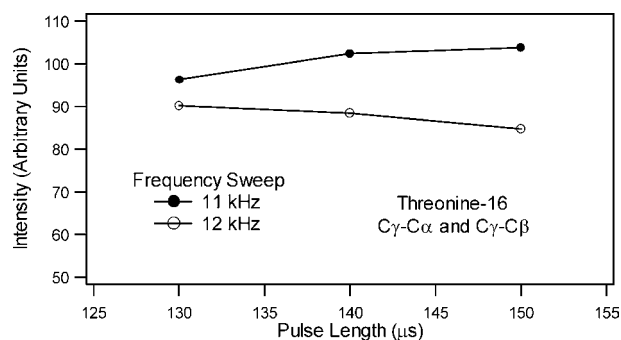

Fig. 14. Threonine-16 Cα + Cβ to Cγ cross-peak intensities with linear frequency sweeps after 144 mixing pulses performed at 600 MHz. The mixing times corresponding to the pulse lengths 130, 140, and 150 μs were 18.72, 20.16, and 21.6 ms, respectively. The phase cycle was MLEV-16 with *XY* phase alternation, and the nominal RF field amplitude was 7.7 kHz.
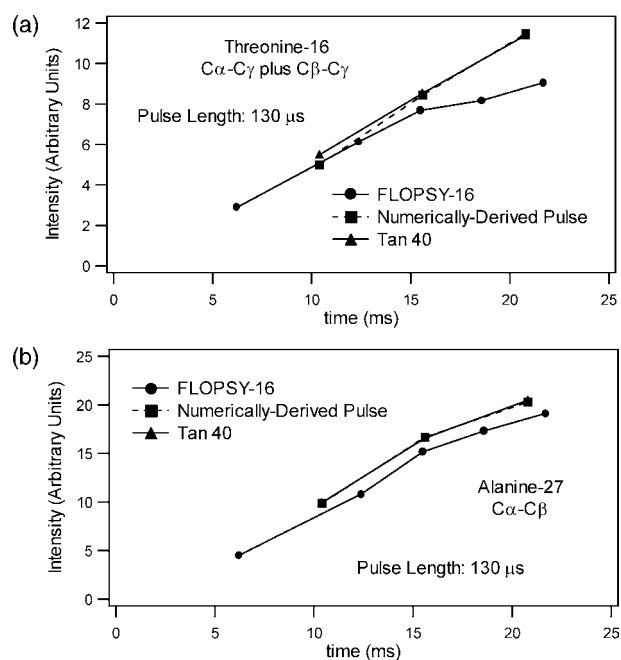

Fig. 15. Experimental cross-peak intensities obtained from mixing experiments performed on a Varian 750 spectrometer. The nominal RF field was 7.7 kHz, the pulse length 130 μs. Both adiabatic pulses exhibit improvements in these isolated two and three spin systems with large chemical shift differences. The advantage of the adiabatic approaches is greater at longer mixing times as predicted by the simulations. In part (a), the Cα–Cγ cross-peak is added to the Cβ–Cγ cross-peak in order to assess total exchange across Cβ–Cγ. In part (b), improved results are also obtained for Ala-27, which has a two spin pair.

full phase cycle, and accordingly it should be kept in mind that the total mixing time is increasing as the pulse length τ is increased. Accordingly, the shortest pulse τ which yields maximum intensity is close to the optimal value.

Using the more tailored pulse shapes given in Figs. 7 and 15, illustrates that the theoretically predicted
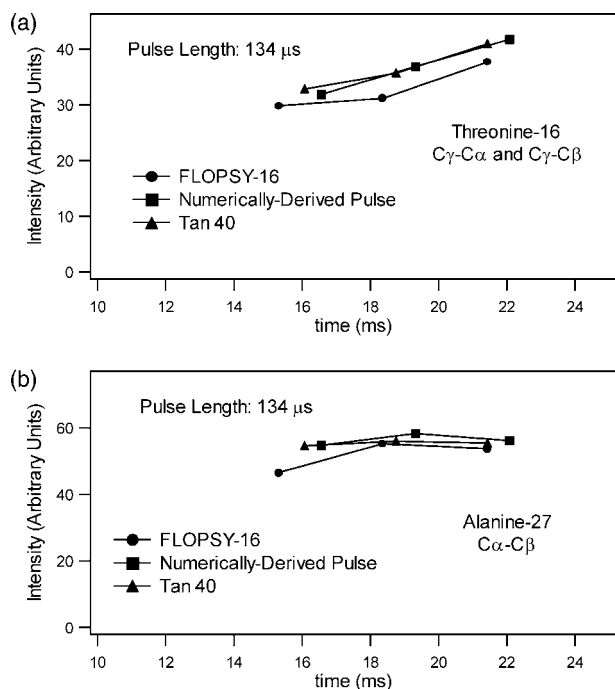
Fig. 16. Experimental cross-peak intensities obtained from mixing experiments performed on a Bruker 600 spectrometer. The nominal RF field was 7.7 kHz, the pulse length 134 μs. Both adiabatic pulses exhibit improvements in the these isolated two and three spin systems with large chemical shift differences, as in the case of 750 MHz magnetic field. The advantage of the adiabatic approaches is greater at longer mixing times as predicted by the simulations. In part (a), the Cα–Cγ cross-peak is added to the Cβ–Cγ cross-peak in order to assess total exchange across Cβ–Cγ. In part (b), improved results are again obtained for Ala-27. For all approaches mixing is more rapid at lower field because of the reduced scaling factor obtained as Δδ increases.
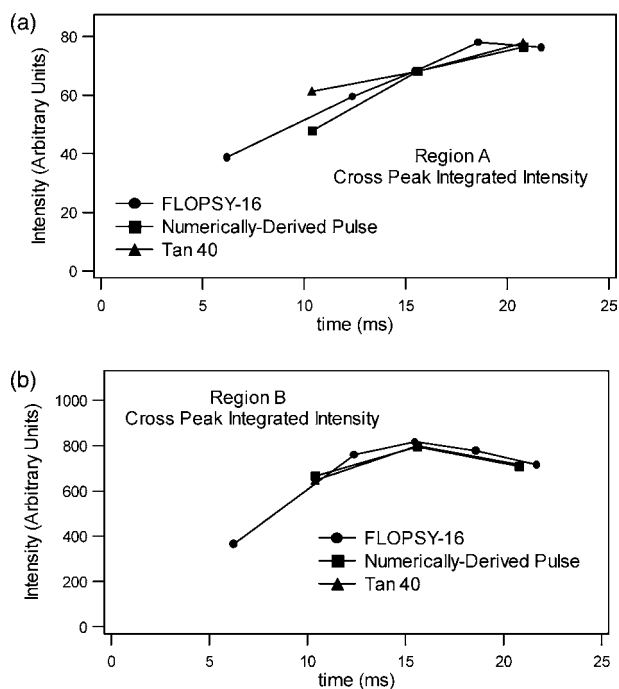
Fig. 17. Regional spectral intensities at 750 MHz magnetic field obtained from regions A and B defined in the spectrum shown in Fig. 13a. Although the curves are similar for the adiabatic and FLOPSY-16 sequences, multiple spin dynamics and averaging over many different spin exchange events are expected to lead to small differences which are hard to predict if both sequences should yield negligible signal losses. (For most of these spectral regions, the values of Δδ are too small to yield significant double-quantum decay using the FLOPSY-16 sequences). In region B, many exchange events are from Cα to other nuclei in the carbon skeleton of amino acids. The slightly reduced total peak intensity seen in this area using adiabatic sequences is likely the result of either multiple spin effects or possibly leakage to aromatic sidechains.

enhancements in the cross-peaks of threonine and alanine, illustrated in Figs. 8–12, are also seen experimentally in the SH3 domain on a Varian 750 MHz machine using a triple resonance probe. The cross-peaks are associated with the Threonine-16 and Alanine-27 residues. The spin pair in Alanine-27 has a chemical shift difference of $\Delta\delta = 6.8$ kHz, as expressed in terms of frequency. It is seen that the long time limit for the total Cα and Cβ to Cγ intensity is reduced using FLOPSY-16 as expected from the reduced exchange efficiency predicted at moderately high $\Delta\delta$. Similar behavior is also seen in Fig. 16 using the Bruker 600 spectrometer. The analytical shape tan 40 yields similar results in all cases and provides an alternative to the numerical approach that is easier to implement. (Indeed, the data given by the tan 40 pulse is mostly overlapping with the points given by the numerical approach in Figs. 15–17). Likewise, in both cases, exchange with adiabatic pulses is more rapid in alanine as predicted by simulations.

In other spectral regions, the results are more complex because of additional multiple spin dynamics and extensive spectral overlap. Indeed, the expected behavior for most other cross-peaks is highly oscillatory, and

the exchange dynamics are much more complex than for the two and three spin systems. Specifically, even if the underlying spin dynamics are similar or on average faster with a given sequence, it is possible to obtain smaller total cross-peak intensities at a given mixing time at times when most of the peaks are decreasing. Fig. 17 illustrates fairly comparable performance in how the total integral of one spectral region behaves as a function of time. In the region B, the slightly lower maximum intensity at longer mixing times seen with the adiabatic sequences likely reflects some leakage of signal to aromatic sidechains, as well as possibly different behavior with multiple spin dynamics in the presence of inhomogeneous RF fields.

5. Discussion

Previous theoretical work aimed at describing magnetization exchange stimulated by RF irradiation has focused on the perspective of continuous-wave fields as reviewed by Glaser and Quant [5]. This approach has

provided much insight into the resonance-offset dependence of composite pulse sequences, although calculations are usually needed to predict mixing behavior quantitatively given the complexity of the spin dynamics. The potential for applying adiabatic pulses to mixing is attractive because of their tolerance to frequency offsets and RF amplitude inhomogeneities [21,23]. However, with adiabatic pulses, the most appropriate model of the pulse sequence is a train of inversion pulses. Accordingly, we have developed a novel theory of how mixing behaves with inversion pulses, and we specialize to the case of linear ramp pulses as a model system, which permits a detailed development of analytical expressions.

Two key results of this novel theoretical approach are that mixing is most efficient using short pulses, which has been previously observed empirically [27], and that amplitude modulation of the pulse diminishes the exchange rate via a reduction in chemical shift scaling. Based on these observations, we have pursued the possibility of applying short adiabatic pulses of constant amplitude. Although the linear ramp "chirp" pulse is a good model system, we have also optimized pulse sequences by testing numerically optimized adiabatic pulses in two and three spin simulations. We have found that it is possible to tune these sequences to the required ^{13}C bandwidth in the useful range from 500 to 750 MHz, and the approach seems amenable to scaling up to higher fields as well.

In practice it is difficult to compete directly with the best known composite pulse sequence, FLOPSY-16, within its bandwidth because it was developed by global numerical optimization via adjustment of multiple parameters [17]. As shown here, its excellent scaling factor seems to come at the expense of total signal decay in the regime of long mixing times because of double-quantum decay. Although this issue has never been discussed previously to our knowledge, the decay of total signal can be inferred even from the original papers which introduced the FLOPSY sequences [17,18]. This limitation does not apply to adiabatic sequences with suitable XY phase cycling. The comparison of the FLOPSY and adiabatic approaches with respect to RF inhomogeneity is also interesting. At lower RF fields, the adiabatic approach is more efficient because of more rapidly decreasing scaling factors found using FLOPSY. At some point higher than the nominal value, however, the scaling behavior becomes superior using FLOPSY.

As demonstrated here, numerically derived adiabatic sequences can be developed which exceed the performance of the FLOPSY sequences at moderately higher values of $\Delta\delta$. At 600 and 750 MHz, however, it seems that the adiabatic approach offers moderate advantages over FLOPSY for the most difficult cross-peaks to obtain in HCCH–TOCSY experiments. For greater ease of implementation, the analytical shape tan 40 is a suitable

substitute. The tan 40 pulse is a type of constant/tan pulse and is also somewhat analogous to the tanh/tan pulses introduced by Garwood and co-workers [28], although here the amplitude of the RF field is constant. Interestingly, Peti et al. have already applied the tanh/tan approach to ^{13}C–^{13}C exchange over the aliphatic bandwidth [27]. The tanh/tan pulse [28] is particularly time-efficient compared to alternatives such as the sech/tanh pulse [42]. Accordingly, it is a well-suited choice among the numerous amplitude-modulated adiabatic waveforms which are available. According to the calculations of Peti and co-workers [27], however, the tanh/tan and related BIR approaches are not as broad-banded as FLOPSY-16 with respect to $\Delta\delta$ for the ^{13}C–^{13}C application. In ^{1}H–^{1}H mixing, on the other hand, where the mixing times are typically longer and the phase cycle can be extended, the tanh/tan pulse can be the basis of a sequence which is theoretically as efficient as FLOPSY [27]. An important theoretical disadvantage of amplitude-modulated waveforms is that chemical shift scaling is less efficient during periods when reduced RF power is applied. More generally, it appears that relaxation of the adiabatic condition leads to shorter pulses which may be advantageous for mixing. Semi-adiabatic inversion pulses with constant amplitude, such as the BIP pulse of Shaka and co-workers [47] and the pulses discussed here, provide alternative approaches which maximize chemical shift scaling and could prove useful for mixing applications.

In the future, when experiments are performed at 900 MHz and above for maximum sensitivity and resolution, the FLOPSY-16 sequence will become increasingly inadequate when chemical shift differences are especially large, as in alanine and threonine. Unlike FLOPSY, the range of the adiabatic sequences can be scaled by designing new pulses which cover a larger bandwidth. Although it should usually be possible to generate practical exchange sequences using the principles established in Section 2, it seems unlikely that a superior scaling factor to the composite pulse approach can be simultaneously preserved at small values of $\Delta\delta$ with greater extension of the total bandwidth. Moderately slower exchange at small values of $\Delta\delta$, however, is unlikely to have much practical significance, and it will likely be preferable to apply adiabatic sequences which can generate all possible cross-peaks in the very high field regime.

There are several interesting avenues to pursue in the future. Specifically for the ^{13}C–^{13}C aliphatic mixing problem pursued here, it would be helpful to understand the multiple spin dynamics better in networks of greater than three spins. These calculations would increase the current understanding of how to optimize the application of homonuclear mixing sequences to multiple spin systems which exhibit many different chemical shifts. For structural biology applications, these studies would

be most helpful if applied directly to the amino acids and nucleic acids found in biopolymers. Likewise, for application to larger proteins, the inclusion of relaxation effects in simulations would be helpful and could be very important in choosing the best pulse sequence. In this work we have examined longitudinal exchange in a 7 kDa protein. However, given fast relaxation of higher order coherences, it is likely that longitudinal exchange is also the best approach in larger proteins, although this issue has not been explicitly studied to our knowledge. As a practical matter, difficulty in assigning $^1H\alpha$ shifts is a commonly encountered problem in larger proteins (>20 kDa) due to rapid transverse spin relaxation. Furthermore, in larger proteins, the most promising approach to sidechain assignment is to apply $^{13}C–^{13}C$ exchange experiments with ^{15}NH filtering. An example is the HCCONH experiment [12]. Future work could build on the principles established here to pursue this interesting application more explicitly. The theoretical framework developed here is highly general and should also be applicable to $^1H–^1H$ TOCSY experiments, which are often applied to assign aromatic sidechains in proteins, and alternative adiabatic approaches to the $^{13}C–^{13}C$ aliphatic exchange problem. In addition, there is the possibility of extending this approach to $^{13}C–^{13}C$ exchange between aliphatic and aromatic ^{13}C resonances, which are separated by approximately $\Delta\delta \approx 17$ kHz at 750 MHz. Such an application is likely feasible if higher RF power could be applied routinely using future probe designs.

6. Conclusion

This paper has introduced a novel theoretical framework for understanding how coherence exchange can be stimulated via trains of inversion pulses. This theory was also extended to the case of adiabatic inversion pulses with arbitrary shape and carried out analytically for the case of a linear frequency sweep with constant RF amplitude. This pulse was found to be a good model for numerically generated constant amplitude pulses which are directly applicable to $^{13}C–^{13}C$ exchange at high magnetic field. Although the additional enhancement in exchange efficiency is moderate for the ^{13}C aliphatic application discussed here, we have shown that our approach is superior to the best known composite pulse technique for the most widely separated $^{13}C–^{13}C$ pairs at 600 and 750 MHz. The simpler analytical shape tan 40 is able to provide comparable results. At typical RF field strengths, increasing signal losses and limitations on the maximum bandwidth are predicted with composite pulse sequences such as FLOPSY-16 as the magnetic field is increased. Accordingly, the more flexible framework provided by adiabatic pulses will likely give them an increasingly decisive advantage at higher fields.

The principles established here are of very general applicability in the analysis of adiabatic pulse sequences and include an improved understanding of the roles of pulsing rate, chemical shift scaling, and double-quantum contamination. The role of the latter effect in attenuating the cross-peaks in composite pulse mixing sequences was also introduced and is an important limitation of the FLOPSY sequence at larger bandwidth. The principles introduced here should be of general utility in the design of adiabatic mixing sequences in a variety of contexts.

Appendix A

A.1. Approximate calculations of the scaling factor with a linear ramp pulse

Optimization of the value of α in Eq. (2.33) requires that the following integral be set to zero:

$$\int_0^{\tau/2} dt\{\chi(t) - \Delta\delta \cdot \alpha t\} \cdot \{\Delta\delta \cdot \alpha t\} = 0. \quad (A.1)$$

For the linear ramp pulse, the phase factor can be integrated analytically:

$$\chi(t) = \Delta\delta \int_0^t dt' \frac{(\delta_{max} - kt')}{\sqrt{(\delta_{max} - kt')^2 + v_{RF}^2}}$$

$$= \Delta\delta \int_{\delta(t)}^{\delta_{max}} \frac{d\delta}{2k} \frac{2\delta}{\sqrt{\delta^2 + v_{RF}^2}}$$

$$= \frac{\Delta\delta\tau}{2\delta_{max}} \left\{ \sqrt{\delta_{max}^2 + v_{RF}^2} - \sqrt{(\delta_{max} - kt)^2 + v_{RF}^2} \right\}. \quad (A.2)$$

With this expression for the accumulated phase, the condition given by Eq. (A.1) leads to the expression:

$$\int_0^{\tau/2} dt\, t \left\{ \alpha t - \frac{\tau}{2\delta_{max}} \left(\sqrt{\delta_{max}^2 + v_{RF}^2} \right. \right.$$
$$\left. \left. - \sqrt{(\delta_{max} - kt)^2 + v_{RF}^2} \right) \right\} = 0, \tag{A.3}$$

which in turns yields:

$$\alpha \int_0^{\tau/2} dt\, t^2 = \frac{\tau}{2\delta_{max}} \int_0^{\tau/2} dt\, t \left\{ \sqrt{\delta_{max}^2 + v_{RF}^2} \right.$$
$$\left. - \sqrt{(\delta_{max} - kt)^2 + v_{RF}^2} \right\}, \tag{A.4}$$

and accordingly

$$\alpha = \left(\frac{2}{\tau} \right)^3 \frac{3\tau}{2\delta_{max}} \left\{ \frac{1}{2} \left(\frac{\tau}{2} \right)^2 \sqrt{\delta_{max}^2 + v_{RF}^2} \right.$$
$$\left. - \int_0^{\tau/2} dt\, t \sqrt{(\delta_{max} - kt)^2 + v_{RF}^2} \right\}. \tag{A.5}$$

The remaining integral can be solved as follows

$$\int_0^{\tau/2} dt\, t \sqrt{(\delta_{max} - kt)^2 + v_{RF}^2}$$
$$= \frac{-1}{k} \int_0^{\tau/2} dt (\delta_{max} - kt) \sqrt{(\delta_{max} - kt)^2 + v_{RF}^2}$$
$$+ \frac{1}{k} \int_0^{\tau/2} dt\, \delta_{max} \sqrt{(\delta_{max} - kt)^2 + v_{RF}^2}$$
$$= \frac{1}{3k^2} \left\{ v_{RF}^3 - (\delta_{max}^2 + v_{RF}^2)^{3/2} \right\}$$
$$+ \frac{\tau}{2} \int_0^{\tau/2} dt \sqrt{(\delta_{max} - kt)^2 + v_{RF}^2}$$
$$= \frac{1}{3} \left(\frac{\tau}{2\delta_{max}} \right)^2 \left\{ v_{RF}^3 - (\delta_{max}^2 + v_{RF}^2)^{3/2} \right\}$$
$$+ \frac{1}{2} \left(\frac{\tau}{2} \right)^2 \sqrt{\delta_{max}^2 + v_{RF}^2} + \frac{1}{2} \left(\frac{\tau}{2} \right)^2 \frac{v_{RF}^2}{\delta_{max}}$$
$$\times \ln \left\{ \frac{\delta_{max}}{v_{RF}} + \sqrt{1 + \frac{\delta_{max}^2}{v_{RF}^2}} \right\}, \tag{A.6}$$

using the solution to the integral $\int_0^{\tau/2} dt$ $\sqrt{(\delta_{max} - kt)^2 + v_{RF}^2}$ provided in Appendix A.2. Substitution of the result given in Eq. (A.6) into Eq. (A.5) leads to the final analytical expression for α, also given in Eq. (2.34):

$$\alpha = \left\{ \left(1 + \frac{v_{RF}^2}{\delta_{max}^2} \right)^{3/2} - \frac{v_{RF}^3}{\delta_{max}^3} \right\}$$
$$- \frac{3v_{RF}^2}{2\delta_{max}^2} \ln \left\{ \frac{\delta_{max}}{v_{RF}} + \sqrt{1 + \frac{\delta_{max}^2}{v_{RF}^2}} \right\}. \tag{A.7}$$

A.2. Calculation of the net precession angle during a linear ramp pulse

The integral of Eq. (2.36) is solved via a change of variables using the identities $\delta(t) = \delta_{max} - kt$ and $\delta_{max} = k\tau/2$:

$$\Omega = \int_0^\tau dt \sqrt{\delta^2(t) + v_{RF}^2}$$
$$= \frac{1}{2} \int_0^{\tau/2} dt \sqrt{(\delta_{max} - kt)^2 + v_{RF}^2}$$
$$= \frac{\tau}{\delta_{max}} \int_0^{\delta_{max}} d\delta \sqrt{\delta^2 + v_{RF}^2}, \tag{A.8}$$

followed by application of the following known solution to the integral [48]:

$$\int dx \sqrt{x^2 + a^2} = \frac{1}{2}x\sqrt{x^2 + a^2} + \frac{1}{2}a^2 \ln \left\{ x + \sqrt{x^2 + a^2} \right\}. \tag{A.9}$$

The final result can be expressed as follows when $v_{RF} > 0$:

$$\Omega = \frac{\tau}{\delta_{max}} \left\{ \frac{1}{2} \delta_{max} \sqrt{\delta_{max}^2 + v_{RF}^2} + \frac{1}{2} v_{RF}^2 \right.$$
$$\times \ln \left\{ \delta_{max} + \sqrt{\delta_{max}^2 + v_{RF}^2} \right\} - \frac{1}{2} v_{RF}^2 \ln \left\{ \sqrt{v_{RF}^2} \right\} \right\}$$
$$= \left\{ \frac{1}{2} \sqrt{\delta_{max}^2 + v_{RF}^2} + \frac{v_{RF}^2}{\delta_{max}} \right.$$
$$\left. \times \ln \left[\frac{\delta_{max}}{v_{RF}} + \sqrt{1 + \frac{\delta_{max}^2}{v_{RF}^2}} \right] \right\} \cdot \tau. \tag{A.10}$$

References

[1] J. Cavanagh, W.J. Fairbrother, A.G. Palmer III, N.J. Skelton, Protein NMR Spectroscopy: Principles and Practice, Academic Press, San Diego, CA, 1996.
[2] L. Braunschweiler, R.R. Ernst, J. Magn. Reson. 53 (1983) 521.
[3] A. Bax, D.G. Davis, J. Magn. Reson. 65 (1985) 355.
[4] M.H. Levitt, Prog. NMR Spectrosc. 18 (1986) 61.
[5] S.J. Glaser, J.J. Quant, Adv. Magn. Reson. 19 (1996) 60.
[6] A. Bax, G.M. Clore, A.M. Gronenborn, J. Magn. Reson. 88 (1990) 425.
[7] E.T. Olejniczak, R.X. Xu, S.W. Fesik, J. Biomol. NMR 2 (1992) 655.
[8] T.M. Logan, E.T. Olejniczak, R.X. Xu, S.W. Fesik, FEBS Lett. 314 (1992) 413.
[9] G.T. Montelione, B.A. Lyones, S.D. Emerson, M. Tashiro, J. Am. Chem. Soc. 114 (1992) 10974.
[10] S. Grzesiek, A. Bax, J. Biomol. NMR 3 (1993) 185.
[11] K. Pervushin, R. Roland, G. Wider, K. Wuthrich, Proc. Natl. Acad. Sci. USA 94 (1997) 12366.
[12] K.H. Gardner, R. Konrat, M.K. Rosen, L.E. Kay, J. Biomol. NMR 8 (1996) 351.
[13] Y. Lin, G. Wagner, J. Biomol. NMR 15 (1999) 227.

[14] M. Rance, J. Magn. Reson. 74 (1987) 557.

[15] A.J. Shaka, C.J. Lee, A. Pines, J. Magn. Reson. 77 (1988) 274.

[16] S.P. Rucker, A.J. Shaka, Mol. Phys. 68 (1989) 509.

[17] M. Kadkhodaie, O. Rivas, M. Tan, A. Mohebbi, A.J. Shaka, J. Magn. Reson. 91 (1991) 437.

[18] A. Mohebbi, A.J. Shaka, Chem. Phys. Lett. 178 (1991) 374.

[19] J. Baum, R. Tycko, A. Pines, Phys. Rev. A 32 (1985) 3435.

[20] A. Tannus, M. Garwood, NMR Biomed. 10 (1997) 423.

[21] M. Garwood, L. DelaBarre, J. Magn. Reson. 153 (2001) 155.

[22] E. Kupce, P. Schmidt, M. Rance, G. Wagner, J. Magn. Reson. 135 (1998) 361.

[23] E. Kupce, Methods Enzymol. 338 (2001) 82.

[24] E. Kupce, W. Hiller, Magn. Reson. Chem. 39 (2001) 231.

[25] E. Kupce, P.A. Keifer, M. Delepierre, J. Magn. Reson. 148 (2001) 115.

[26] E. Kupce, R. Freeman, J. Magn. Reson. A 115 (1995) 273.

[27] W. Peti, C. Griesinger, W. Bermel, J. Biomol. NMR 18 (2000) 199.

[28] T. Hwang, P. van Zijl, M. Garwood, J. Magn. Reson. 133 (1998) 200.

[29] E. Kupce, poster presentation Adiabatic TOCSY-s at 900 MHz, 43rd Experimental NMR Conference, Asilomar, California, 2002.

[30] A.J. Shaka, J. Keeler, Prog. NMR Spectrosc. 19 (1986) 47.

[31] D. Rosenfeld, S.L. Panfil, Y. Zur, J. Magn. Reson. 129 (1997) 115.

[32] C.J. Hardy, W.A. Edelstein, D. Vatis, J. Magn. Reson. 66 (1986) 470.

[33] V.J. Basus, P.D. Ellis, H.D.W. Hill, J.S. Waugh, J. Magn. Reson. 35 (1979) 19.

[34] R. Fu, G. Bodenhausen, J. Magn. Reson. A 117 (1995) 324.

[35] R. Tycko, A. Pines, J. Guckenheimer, J. Chem. Phys. 83 (1985) 2775.

[36] A.E. Bennett, C.M. Rienstra, J.M. Griffiths, W. Zhen, P.T. Lansbury, R.G. Griffin, J. Chem. Phys. 108 (1998) 9463.

[37] A.E. Bennett, R.G. Griffin, S. Vega, NMR Basic Principles and Progress: Solid-State NMR IV. Methods and Applications of Solid-State NMR 33 (1994) 1.

[38] M.H. Levitt, D.P. Raleigh, F. Creuzet, R.G. Griffin, J. Chem. Phys. 92 (1990) 6347.

[39] A.E. Bennett, J.H. Ok, S. Vega, R.G. Griffin, J. Chem. Phys. 96 (1992) 8624.

[40] U. Haeberlen, J.S. Waugh, Phys. Rev. 175 (1968) 453.

[41] K. Ugurbil, M. Garwood, A.R. Rath, J. Magn. Reson. 80 (1988) 448.

[42] Y.A. Tesiram, M.R. Bendall, J. Magn. Reson. 156 (2002) 26.

[43] E. Kupce, G. Wagner, J. Magn. Reson. B 109 (1995) 329.

[44] C. Slichter, Principles of Magnetic Resonance, Springer, Berlin, 1990.

[45] E. Kupce, R. Freeman, J. Magn. Reson. A 118 (1996) 299.

[46] J. Li, K. Nishizawa, W. An, R.E. Hussey, F.E. Lialios, R. Salgia, R. Sunder-Plassman, E. Reinherz, EMBO J. 24 (1998) 7320.

[47] M.A. Smith, H. Hu, A.J. Shaka, J. Magn. Reson. 151 (2001) 269.

[48] Ruth Zucker, in: M. Abramowitz, I.A. Stegun (Eds.), Handbook of Mathematical Functions, with Formulas, Graphs, and Mathematical Tables, National Bureau of Standards, Washington, 1974.